Journal of Wind Engineering & Industrial Aerodynamics 209 (2021) 104484

Contents lists available at ScienceDirect

Journal of Wind Engineering & Industrial Aerodynamics

journal homepage: www.elsevier.com/locate/jweia

A comparative study of wind-induced dynamic response models of long-span bridges using artificial neural networks, support vector regression and buffeting theory

Dario Fernandez Castellon *, Aksel Fenerci, Ole Øiseth

Department of Structural Engineering, Norwegian University of Science and Technology, Trondheim, Norway

ARTICLE INFO

Keywords:
Long-span bridges
Full-scaled measurements
Buffeting response
Multilayer perceptron
Supporting vector regression

ABSTRACT

Long-span cable-supported bridges are structures susceptible to high dynamic responses due to the buffeting phenomenon. The current state-of-the-art method for buffeting response estimation is the buffeting theory. However, previous research has shown discrepancies between buffeting theory estimates and full-scale measured response, revealing a weakness in the theoretical models. In cases where wind and structural health monitoring data are available, machine learning algorithms may enhance the buffeting response estimation speed with less computational effort by bypassing the analytical model's assumptions. In this paper, multilayer perceptron and support vector regression models were trained with synthetic and full-scale measured data from the Hardanger Bridge. The analytical response was also computed from buffeting theory applied to a finite element model of the bridge, and the estimates are compared. The prediction accuracy was evaluated with the normalized root mean square error, the mean absolute percent error and the coefficient of determination (R2). The machine learning models trained with synthetic datasets achieved very high accuracy with normalized root mean square errors ranging from 1.46E-04 to 7.21E-03 and are therefore suitable for efficient surrogate modeling. Further, the support vector regression model trained with the full-scale measured dataset achieved the best accuracy compared with the other methods.

1. Introduction

The current state-of-the-art method for buffeting response prediction of long-span bridges is to use buffeting theory, which was first introduced by (Davenport A., 1962). Since Davenport's early works, the theory has been further developed by many researchers. Current advanced models are based on finite element formulations, which can account for unsteady self-excited forces (Scanlan and Tomko, 1971) (Davenport A., 1962) (Jain et al., 1996), nonlinearities (Diana et al., 2008) (Diana et al., 2005) (Chen and Kareem, 2003), skew winds (Zhu and Xu, 2005) and non-stationary winds (Hu, Xu, & Huang, Typhoon-induced non-stationary buffeting response of long-span bridges in complex terrain, 2013) (Hu et al., 2017). However, owing to the recent emergence of a large number of structural health monitoring (SHM) projects on prominent suspension bridges around the world, researchers have reported discrepancies in dynamic responses between their analytical predictions based on buffeting theory and the SHM data (Bietry et al., 1995) (Macdonald, 2003) (Xu and Zhu, 2005) (Cheynet et al., 2016) (Fenerci and Øiseth, 2017). Such discrepancies expose the weakness of analytical modeling of the complex phenomenon, presumably due to several assumptions inherent to buffeting theory.

In cases where monitoring data are present, an alternative solution may be found in using data-driven models based on machine learning. Machine learning is the scientific discipline of developing *algorithms* that can *learn* from data, which allows *prediction* based on existing trends within datasets. Therefore, such algorithms offer an approximation of a process by bypassing the complexity of its physics (Bishop C. M., 2006) (Alpaydin, 2020). The potential of machine learning algorithms in civil engineering applications has been recognized by many researchers, and their use is becoming increasingly common as more user-friendly software is becoming available. For instance, machine learning algorithms can be trained to replace the analytical load-response relationships by means of surrogate models. Such a strategy saves significant computational effort when many simulations are needed. Recently, such successful efforts have also been presented in the wind engineering community, (Fang et al., 2020) compared the capabilities of three machine learning surrogate models trained with a simulated dataset of

* Corresponding author.
E-mail address: dario.r.f.castellon@ntnu.no (D.F. Castellon).

https://doi.org/10.1016/j.jweia.2020.104484
Received 7 September 2020; Received in revised form 25 November 2020; Accepted 4 December 2020
Available online 24 December 2020

Nomenclature

$\boldsymbol{Y}$	Machine learning output dataset
$\boldsymbol{X}$	Machine learning Input dataset
y_j^k	Output of a generic node
x_i^k	Input of a generic node
ϑ_j^k	Bias of a generic node
ε	SVR tolerance margin
C	Box constraint
α_i, α_i^*	Lagrange multipliers
$w_{i,j}^k$	Weight of a generic connection between two nodes
ξ_i, ξ_i^*	Slack variables
$\boldsymbol{r}$	Displacement vector in Cartesian coordinates
$\boldsymbol{\Phi}, \boldsymbol{\phi}_n$	Vibration modes
$\boldsymbol{\eta}$	Generalized coordinates
$\boldsymbol{M}$, $\boldsymbol{C}$, $\boldsymbol{K}$	Mass, damping and stiffness matrices, respectively
$\boldsymbol{Q}_n$	Wind load vector
$E_1E_2E_3$	Unit vector of the global coordinates
$e_1e_2e_3$	Unit vector of the local beam element
$ev_1ev_2ev_3$	Unit vector of the wind element coordinates
$\boldsymbol{T}_{G2Le}$	Transformation from global to local beam element
$\boldsymbol{T}_{G2Lw}$	Transformation from global to local wind element
$\boldsymbol{T}_{Lw2Le}$	Transformation from a local wind element to a local beam element
$\boldsymbol{T}_{E2S}$	Assembly matrix from local DOF to global DOF
q	Element wind load vector
$\boldsymbol{B}_q$	Buffeting load coefficient matrix
$\boldsymbol{V}_{Lw}$	Local wind velocity vector
D, B	Height and width of the girder
C_D C_L C_M	Force coefficients
R	Autocorrelation function
$\boldsymbol{S}$	Auto or cross-spectral density matrix
Coh	Square root of the coherence function
ρ	Air density
A_n	Spectral quantities
z	Height above the ground
$\boldsymbol{H}$	Frequency response matrix
σ_y σ_z σ_θ	RMS of the structural response
$\chi, \Delta\chi$	Span-wise coordinate
V	Mean wind speed
I_n	Turbulence intensity
K_n	Decay coefficient
α	Vertical angle of attack
α_r, β_r	Rayleigh coefficients
ω, f	Circular and ordinary frequency

Subscripts

ae	Aerodynamic
Buff	Buffeting
Le	Local beam element
Se	Self-excited
Tot	Total
0	Still-air
u, w	Wind direction
r	response
k	Generic layer
i,j	Generic neuron or data sample index
y,z,θ	Horizontal, vertical and torsional responses

Superscripts

$\widehat{\blacksquare}$	Model estimation
$\overline{\blacksquare}$	Constant value, mean or specific for the case
$\tilde{\blacksquare}$	Modal property
$\dot{\blacksquare}$	Derivative with respect to time
$\blacksquare'$	Derivative
$\blacksquare^*$	Complex conjugate
$\blacksquare^{-1}$	Matrix inverse
$\blacksquare^T$	Matrix transpose

Functions

$g(\blacksquare)$	Activation function
$f(\blacksquare)$	governing function
$L(\blacksquare)$	Loss or cost function
$K(\blacksquare)$	Kernel function
$N(\blacksquare)$	Shape function

Abbreviations

SVR	Supporting vector regression
ANN	Artificial neural network
MLP	Multilayer perceptron
WIV	Wind induced vibration
R2	Coefficient of determination
MAPE	Mean average percentual error
RMS	Root mean square
RMSE	Root mean square error
NRMSE	Normalized Root mean squared error
BFT	Buffeting theory
CFD	Computational fluid dynamics
KKT	Karush–Kun–Tucker conditions
CLHS	Correlated latin hypercube sampling
SD	Standard Deviation

non-stationary wave and wind loads of a cable-stayed bridge to improve the efficiency of the response estimation. (Bernardini et al., 2015) proposed an alternative to wind tunnel testing based on surrogate models for computational fluid dynamics (CFD)-based aerodynamic shape optimization of bidimensional profiles using an evolutionary algorithm to update ordinary kriging surrogates. Furthermore (Wu and Kareem, 2011), showed how machine learning can be used to simulate complex nonlinearities in aerodynamic behavior by developing an approach to model aerodynamic nonlinearities in the time domain utilizing an artificial neural network (ANN) framework with embedded cellular automata (CA) applied to the hysteretic nonlinear behavior of aerodynamic systems, (Wang and Wu, 2020) proposed a knowledge-enhanced deep learning (KEDL) algorithm to simulate wind-induced linear/nonlinear structural dynamic responses in simulated dynamic systems. (Le and Caracoglia, 2020) used simulated datasets of a tornado-like wind field to develop an ANN-based surrogate model to approximate the structural fragilities of vertical structures subjected to tornadic wind loads. Surrogate models of flutter derivatives with ANN models trained with wind tunnel test data have been reported by (Chen et al., 2008) and (Rizzo and Caracoglia, 2020), while (Cid Montoya et al., 2018) developed a kriging surrogate model from CFD-based aeroelastic characterization of a bridge cross section and validated it with wind tunnel test measurements. (Nieto et al., 2020) extended the CFD-based kriging surrogate modeling approach proposed by (Cid Montoya et al., 2018) to assess the flutter response of bridges with twin-deck cross-sections. Additionally, the potential of machine learning to enhance automated response prediction tools from SHM systems is promising. Full-scale measurements of wind responses in bridges have recently been used for training machine learning algorithms, (Li et al., 2018) estimated vortex-induced vibrations on full-scale measured data of a cable-stayed bridge with machine learning, while (Wang et al., 2020) trained an ensemble model comprising a random forest (RF), long-short term memory (LSTM), and

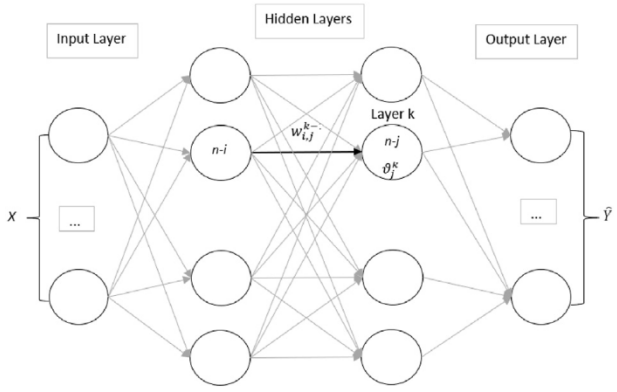

Fig. 1. Architecture of an ANN

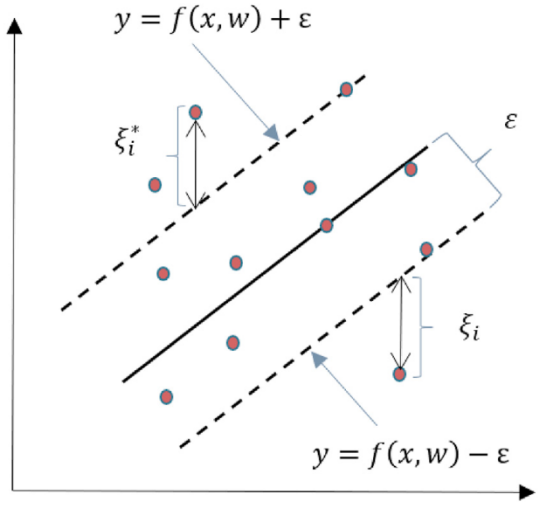

Fig. 2. Schematic representation of SVR with slack variables.

Gaussian process regression (GPR) with measured wind data from the cable-stayed Sutong Yangtze River Bridge in China to forecast wind gusts affecting traffic operations. However, neither of these directly addressed the effect of buffeting responses. Therefore, many uncertainties must be explored as there are no relevant studies based on full-scale measurements for buffeting response estimation in long-span bridges. The deployment and operativity of machine learning algorithms in this field are among the primary challenges to assess. Nonetheless, the effectiveness of machine learning tools shall be explored in terms of which type of algorithm yields better estimates and whether it can provide any improvement with respect to the existing analytical models.

Therefore, this study intends to provide further insight toward understanding the buffeting phenomena of long-span bridges by implementing machine learning algorithms trained with full-scale monitoring data. To address this aim, long-term wind and acceleration monitoring data from the Hardanger Bridge in Norway are used. Two different machine learning techniques, namely, support vector regression (SVR) and multilayer perceptron (MLP) models, are used to model the wind-response relationship. First, the models are trained using analytical predictions to test their capabilities. The remarkable accuracy of these models in predicting the analytical response suggests surrogate modeling based on machine learning is certainly a viable option in cases where many simulations are needed. Owing to the confidence gained from synthetic data, the models are then trained using full-scale monitoring data. The results show that reasonably accurate predictions of the dynamic response can be reached by using only wind characteristics data. Finally, the predictions based on machine learning algorithms are compared to the analytical results based on buffeting theory.

2. Machine learning methods for buffeting response prediction

2.1. Modeling the wind-response relationship

The buffeting responses of long-span suspension bridges can be predicted analytically using buffeting theory. In the frequency domain, the wind field is modeled by a cross-spectral density matrix defined by the time-averaged wind speed and several turbulence-related parameters. Then, by means of buffeting theory, the root mean square (RMS) of the dynamic response components are obtained.

Here, an alternative data-driven approach using machine learning algorithms will be used to estimate the dynamic response of a long-span suspension bridge. The objective of machine learning is to find patterns within a dataset to then make predictions based on the discovered patterns. Applied to buffeting response estimation, machine learning can approximate the unknown function, $f(X)$, between the wind parameters of the cross-spectral density function and the RMS of the bridge's dynamic responses, defined as the input tensor (X) and the target tensor (Y), respectively. Machine learning algorithms fit $f(X)$ over a large amount of data samples in the three different stages of the so-called learning procedure: training, validation, and testing. Hence, the dataset is divided into training, validation, and testing sets. The training dataset comprises the samples used for fitting the model parameters (Ripley, 1996). The validation dataset comprises samples that are used to evaluate the performance of the fitted trained model (James et al., 2013) and subsequently adjust the model hyperparameters (Ripley, 1996). Finally, the test dataset comprises the samples that follows the same probabilistic distribution of the training dataset but has not been fed into the model, therefore evaluating the generalization ability of the model (Ripley, 1996).

Equation (1) shows the machine learning process for the wind-response relationship.

$$\text{Given } X_i \text{ and } Y_i \text{ Find } f(X) \therefore Y \cong f(X)\ \widehat{Y}_j = f\left(X_j\right) \tag{1}$$

The indexes i *and* j represent the training and testing datasets, respectively.

Two different machine learning models were implemented. The first model is an ANN called an MLP, which was use because of its simplicity and common use in the literature. The second was SVR, which was used because of its remarkable generalization ability and performance (Awad and Khanna, 2015). Further details will be given in this section.

2.2. Artificial neural networks (ANN) – multilayer perceptron (MLP) model

An ANN is an algorithm that mimics the functioning of biological brains by assembling *layered neurons connected* to each other. A neuron (also known as a unit or node) is an operational entity that stores and distributes information (Rosenblatt, 1958). The neurons are organized in sets called layers, and the neurons within one layer are connected to those in the subsequent layer. The layer connections transmit information within the neurons and, mathematically, are the arrays governing the transformation relationships. The value of a neuron in an arbitrary layer is the scalar product between its transformation array and the output of the neurons in the previous layer; then, the neuron is activated whenever its value surpasses a certain threshold (Rosenblatt, 1958). The type of neural network used in this study is the so-called MLP (Rosenblatt, 1961), which is schematically shown in Fig. 1.

In Equation (2), y_j^k is the output of the j -th node in the k -th arbitrary layer of an MLP and is related to an activation bias ϑ_j^k and connection weights $w_{i,j}^{k-1}$, where x_i^{k-1} is the value of the i-th node of the previous layer. Then, a nonlinear activation function, $g(x)$, is applied to the result

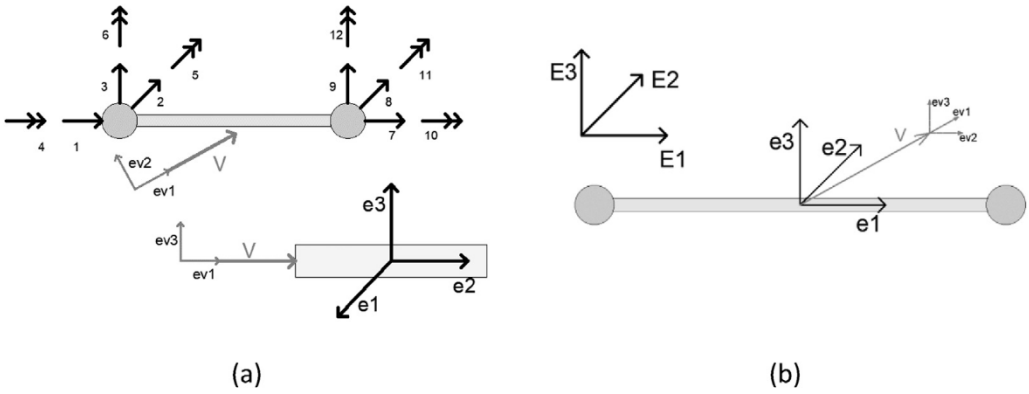

Fig. 3. Local coordinate system of the beam element: (a) DOF of the beam element. (b) Wind actions on the beam element.

$$\boldsymbol{T}_{G2Le} = \begin{bmatrix} \boldsymbol{e}_1^T \\ \boldsymbol{e}_2^T \\ \boldsymbol{e}_3^T \end{bmatrix} \tag{15}$$

$$\boldsymbol{T}_{G2Lw} = \begin{bmatrix} \boldsymbol{ev}_1^T \\ \boldsymbol{ev}_2^T \\ \boldsymbol{ev}_3^T \end{bmatrix} \tag{16}$$

$$\boldsymbol{T}_{Lw2Le} = \boldsymbol{T}_{G2Le}\boldsymbol{T}_{G2Lw}^T \tag{17}$$

Table 1
Range and intervals for the uniform grid simulated training dataset.

Wind Feature	Minimum	Maximum	Number of Intervals
V	4	35	10
σ_u	0.2	5.2	10
σ_w	0.1	2	10
K_u	2.5	15	5
K_w	1.5	25	5

Table 2
Synthetic datasets features summary.

Dataset	Simulation strategy	Distribution	Size
Training uniform	Uniform grid	Uniform	25,000
Training CLHS	CLHS	Observed	3500
Testing CLHS	CLHS	observed	500

(Bishop C. M., 1994). The subsequent operations in matrix notation are presented in Equation (3). The feedforward mapping process (Equation (4)) is then obtained by assembling the abovementioned operations until the model's final M layer is reached and by computing the model estimation of the output $\widehat{Y}$, where $f(X)$ is the process-governing function.

$$y_j^k = g\Big(\sum_{i=1,j=j}^{N} w_{i,j}^{k-1} x_i^{k-1} + \vartheta_j^k\Big) \tag{2}$$

$$Y^k = g\Big\{\big(W_i^{k-1}\big)^T * \ X^{k-1} + \theta^k\Big\} \tag{3}$$

$$\widehat{Y} = f\Big\{\big(W_i^{M-1}\big)^T \ldots g\Big\{\big(W_i^1\big)^T X^1\Big\} + \theta^M\Big\} \tag{4}$$

The actual output of the process or target is known in the training stage. Thus, the ANN performance is obtained by comparing the target with the model estimation with a "loss" function $L(\widehat{y}_j, y_j)$.

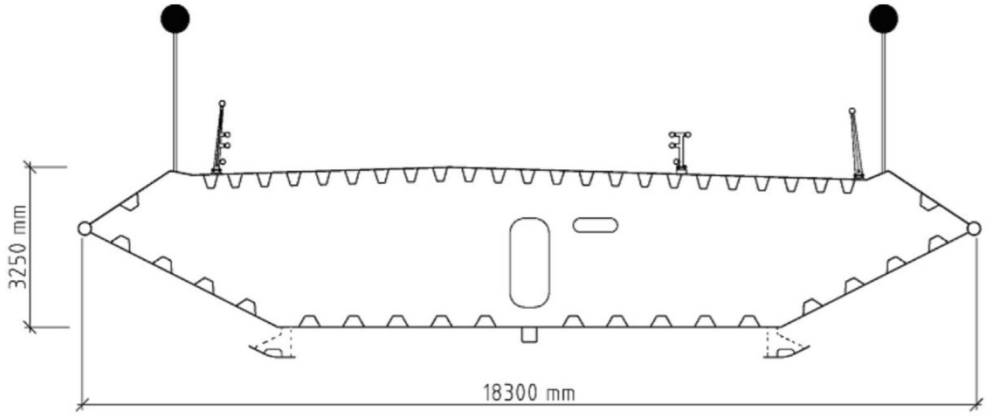

Fig. 4. Cross section of the Hardanger bridge.

Table 3
Natural frequencies of the still-air mode.

Mode	Frequency Hz	Circular Frequency	Damping Ratio	Characteristic
1	0.050	0.315	0.32%	Symmetric lateral vibration of the deck
2	0.098	0.616	0.41%	Asymmetric lateral vibration of the deck
3	0.110	0.694	0.45%	Asymmetric vertical vibration of the deck
4	0.141	0.884	0.54%	Symmetric vertical vibration of the deck
5	0.169	1.062	0.63%	Symmetric lateral vibration of the deck
6	0.197	1.239	0.72%	Symmetric vertical vibration of the deck
7	0.211	1.326	0.76%	Asymmetric vertical vibration of the deck
8	0.225	1.414	0.81%	Symmetric lateral vibration of the cables
9	0.233	1.461	0.84%	Asymmetric lateral vibration of the cables
10	0.234	1.468	0.84%	Asymmetric lateral vibration of the deck and the cables
11	0.244	1.533	0.87%	Symmetric lateral vibration of the deck and the cables
12	0.272	1.709	0.97%	Symmetric vertical vibration of the deck
13	0.293	1.841	1.04%	Asymmetric lateral vibration of the deck
14	0.33	2.073	1.16%	Asymmetric vertical vibration of the deck
15	0.36	2.262	1.27%	Symmetric torsional vibration of the deck

Table 4
Load coefficients from wind tunnel testing

Load Coefficients	$\overline{C}_D$	C'_D	$\overline{C}_L$	C'_L	$\overline{C}_M$	C'_M
Value	1.05	0.00	−0.363	2.2	−0.017	0.786

The mathematical objective of the learning process is to minimize the loss function. This minimization is achieved by sending the estimation error of Equation (4) through all the previous layers within the network; this operation results in an iterative optimization procedure known as backpropagation (Rumelhart et al., 1986). It is worth noting that the backpropagation procedure refers to only the error feeding step and is independent of the optimization algorithm used.

The original input signals are fixed to the dataset; therefore, the only parameters to be updated in each iteration are the network weights and biases. Thus, the optimization problem can be written as Equation (5).

$$find\left(W^{k\in\{1:M-1\}}\ \&\ \theta^{k\in\{1:M\}}\right) \therefore L\left(\widehat{y}_j,\ y_j\right) = \min(L) \tag{5}$$

2.3. Supporting vector regression (SVR) model

SVR is the application of the support vector approximation to a regression problem using an ε-insensitive loss function (Vapnik, 1995). The objective of the tool is to find a function $f(x)$ that, from a given dataset of input and output features $\{x_i,y_i|\ldots|x_n,y_n\}$, approximates y_i with a certain tolerance ε. The regression estimation can be obtained with the linear function shown in Equation (6).

$$f(x) = x^{'} w + \vartheta \tag{6}$$

Introducing the ε-insensitive loss function L equal to zero when the difference between the estimation $f(x)$ and the target is less than ε, a constraint shown in Equation (7) is added to the problem.

$$L(y - f(x,w)) = \begin{cases} 0 & if |y - f(x,w)| \le \varepsilon \\ |y - f(x,w)| & otherwise \end{cases} \tag{7}$$

To make the solution more feasible, the tolerance margin is softened by adding a set of slack variables ξ_i and ξ_i^*, as shown in Fig. 2.

The optimization problem becomes Equation (8), where C is the so-called box constraint, which is a positive-valued parameter that imposes a penalty on the estimations outside the ε-margin and thus helps to balance the accuracy of the model.

$$\begin{aligned} &minimize && \frac{1}{2}w^2 + C\sum_{i=1}^{N}\xi_i + \xi_i^* \\ &with\ constraints: && \begin{cases} y_i - f(x,w) \le \varepsilon + \xi_i \\ f(x,w) - y_i \le \varepsilon + \xi_i^* \\ \xi_i, \xi_i^* \ge 0 \end{cases} \end{aligned} \tag{8}$$

Solving this optimization problem with inequality constraints is equivalent to finding the saddle point in the Lagrange function. By introducing α_n and α_n^* as Lagrange multipliers, the weights (w parameters) can be found by Equation (9), and the model estimation is computed by expanding the so-called support vectors in Equation (10).

$$w = \sum_{i=1}^{N}(\alpha_i - \alpha_i^*)x_i \tag{9}$$

$$f(x) = \sum_{i=1}^{N}(\alpha_i - \alpha_i^*)(x_i^{'}x) + \vartheta \tag{10}$$

The parameters ϑ can be obtained by exploiting the Karush–Kun–Tucker (KKT) conditions (William, 1939) (Kuhn and Tuker, 1951), which state that at the optimal solution, the product between the dual variables and constraints vanishes. Then the constraints of Equation (11) are added to the optimization problem.

$$\begin{aligned} &\alpha_i\left(\varepsilon + \xi_i - y_i + x_i^T w + \vartheta\right) = 0 \\ &\alpha_i^*\left(\varepsilon + \xi_i^* + y_i - x_i^T w - \vartheta\right) = 0 \\ &\xi_i(\mathrm{C} - \alpha_i) = 0 \\ &\xi_i^*\left(\mathrm{C} - \alpha_i^*\right) = 0 \end{aligned} \tag{11}$$

To extend the formulation to nonlinear regression problems, the dot product $(x_i^{'}x)$ must be replaced with a nonlinear mapping function, known as the kernel function $K(x_i^{'}x)$.

$$f(x) = \sum_{i=1}^{N}(\alpha_i - \alpha_i^*)K(x_i^{'}x) + \vartheta \tag{12}$$

3. Training data

3.1. Synthetic data: analytical predictions

Before extending the model to full-scale measurements, it was tested on an ideal case of simulated datasets. The datasets were obtained by simulating random wind fields and calculating the corresponding RMS dynamic response of the bridge using multimode buffeting theory in the frequency domain.

3.1.1. Multimode buffeting theory in the frequency domain

The buffeting response of the bridge was computed in the frequency domain following classical multimode theory (Chen et al., 2000) (Jain et al., 1996) (Katsuchi et al., 1998). The theory requires the following assumptions: The bridge is idealized as a line-like structure, the wind field is approximated as homogenous and stationary, and the wind action

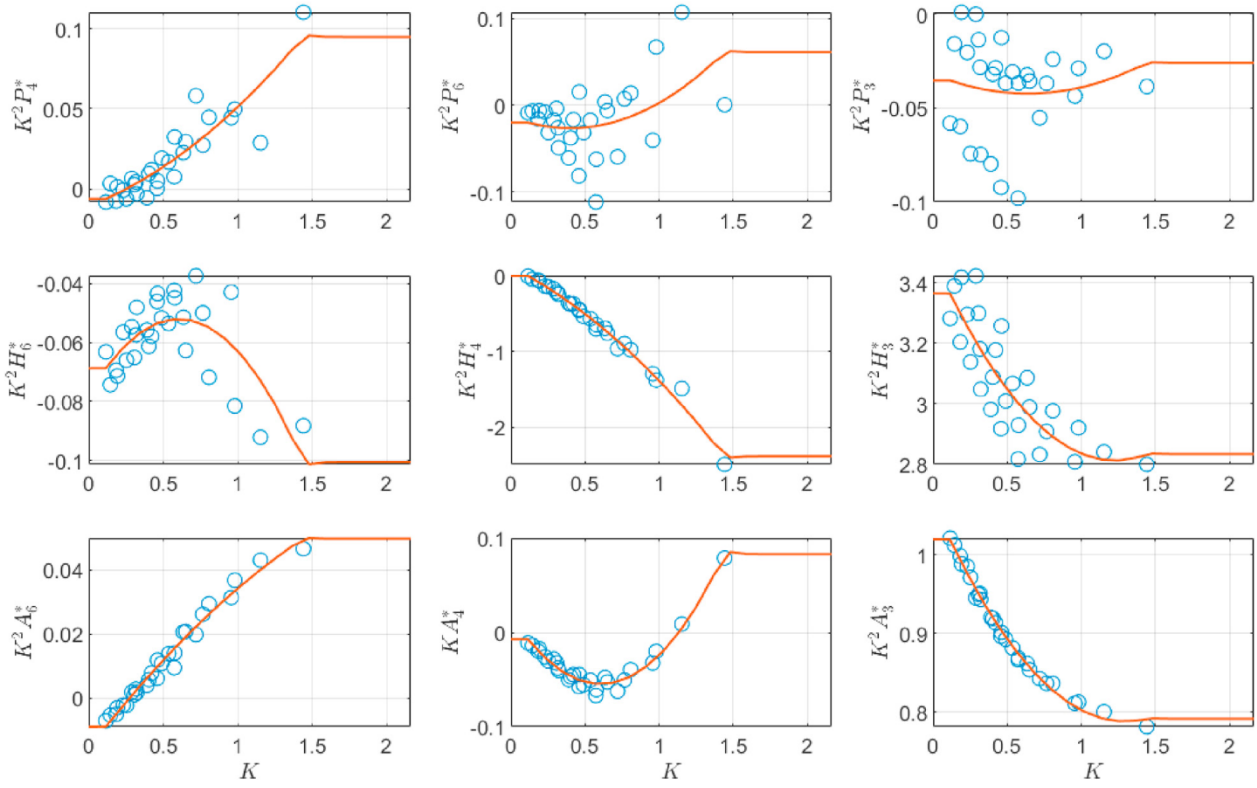

Fig. 5. Dimensionless aerodynamic derivatives related to aeroelastic stiffness as function of reduced frequency. Points are experimental data, continuous line fitted function.

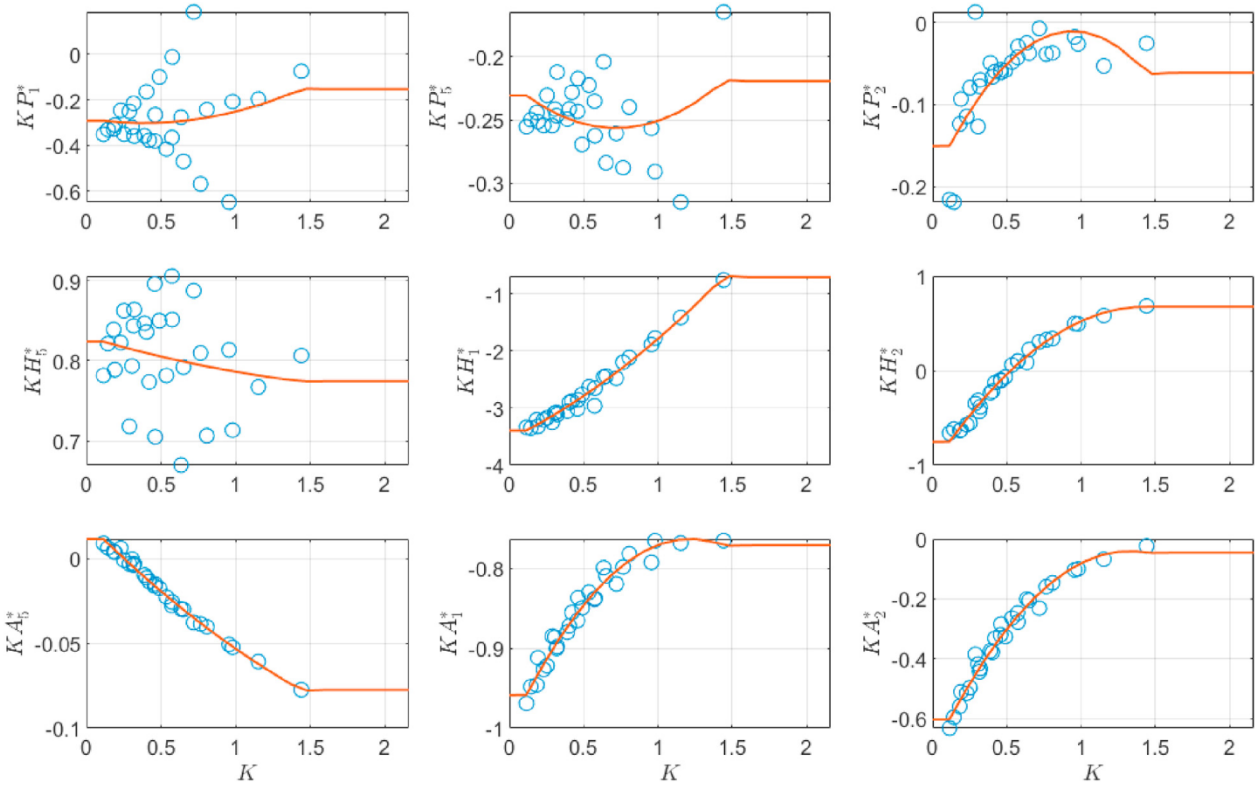

Fig. 6. Dimensionless aerodynamic derivatives related to aeroelastic damping as function of reduced frequency. Points are experimental data, continuous line fitted function.

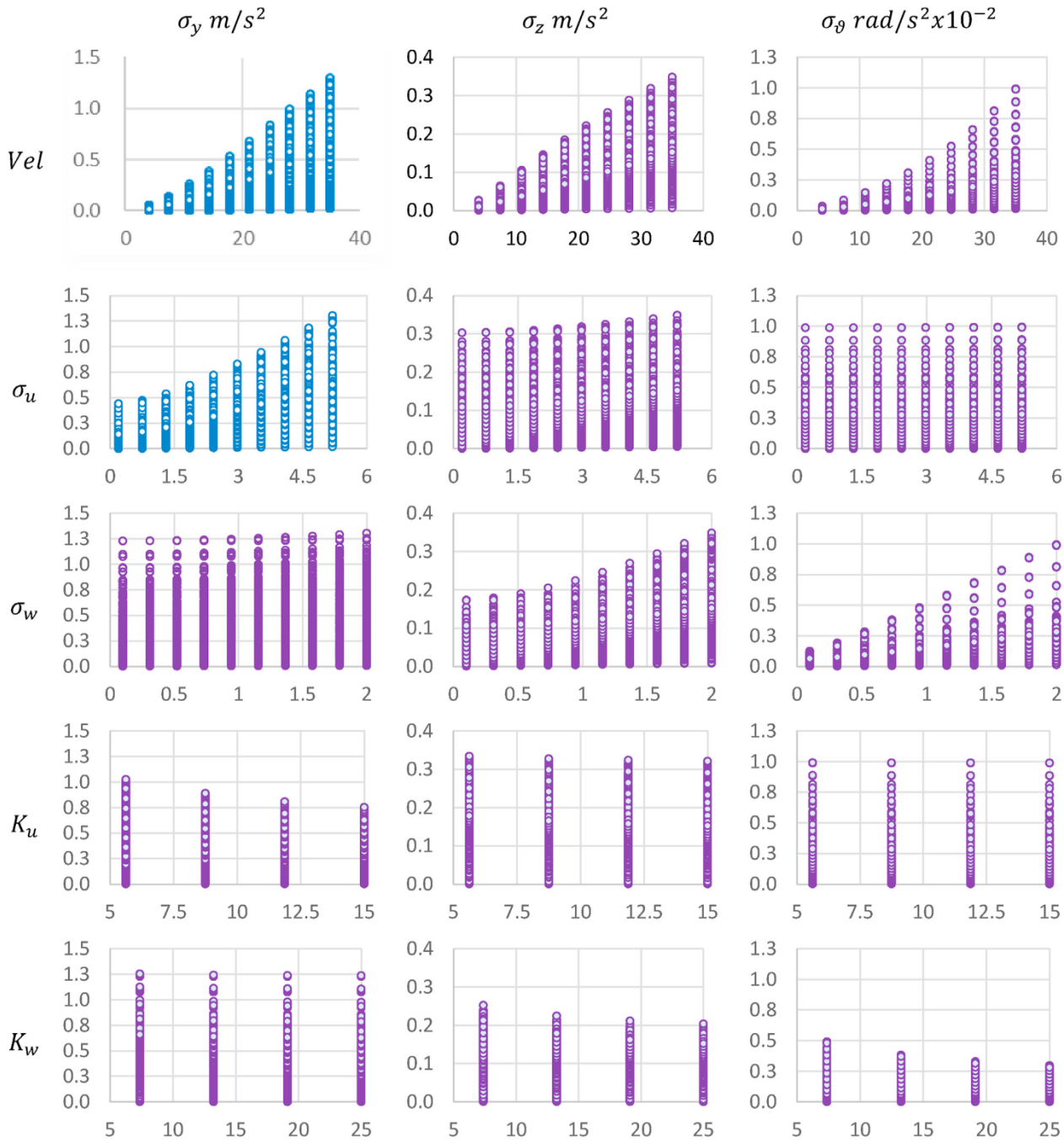

Fig. 7. Uniform grid training dataset (simulated data).

and displacements are referred to as the shear center of the bridge girder and can be separated into a time-invariant mean and a randomly fluctuating part. For surrogate model trained with the synthetic datasets, the aeroelastic forces were computed with the quasi-steady theory. In contrast, aerodynamic derivatives were included in the formulation for the case of comparison with full-scaled measurements. In both cases the experimental data came from the wind tunnel test reported by (Siedziako et al., 2017).

Multimodal theory represents the structural quantities using the mode shapes as generalized coordinates. Then, the structural displacements due to buffeting, $\boldsymbol{r}$, in a Cartesian coordinate system are represented by the sum of the products of the selected natural mode shapes, $\boldsymbol{\Phi}$, and the respective generalized coordinates$\boldsymbol{\eta}$, as in Equation (13).

$$\boldsymbol{r}(\chi,t) = \boldsymbol{\Phi}(\chi)\boldsymbol{\eta}(t)\ \boldsymbol{\Phi}(\chi) = [\,\boldsymbol{\phi}_1 \ldots \boldsymbol{\phi}_i \ldots \boldsymbol{\phi}_N]^T\ \boldsymbol{r}(\chi,t) = [\,\boldsymbol{r}_y\ \boldsymbol{r}_z\ \boldsymbol{r}_\theta]^T\ \boldsymbol{\eta}(t) = [\,\boldsymbol{\eta}_1 \ldots \boldsymbol{\eta}_i \ldots \boldsymbol{\eta}_N]^T\ \boldsymbol{\phi}_i = .[\,\boldsymbol{\phi}_y\ \boldsymbol{\phi}_z\ \boldsymbol{\phi}_\theta]^T \tag{13}$$

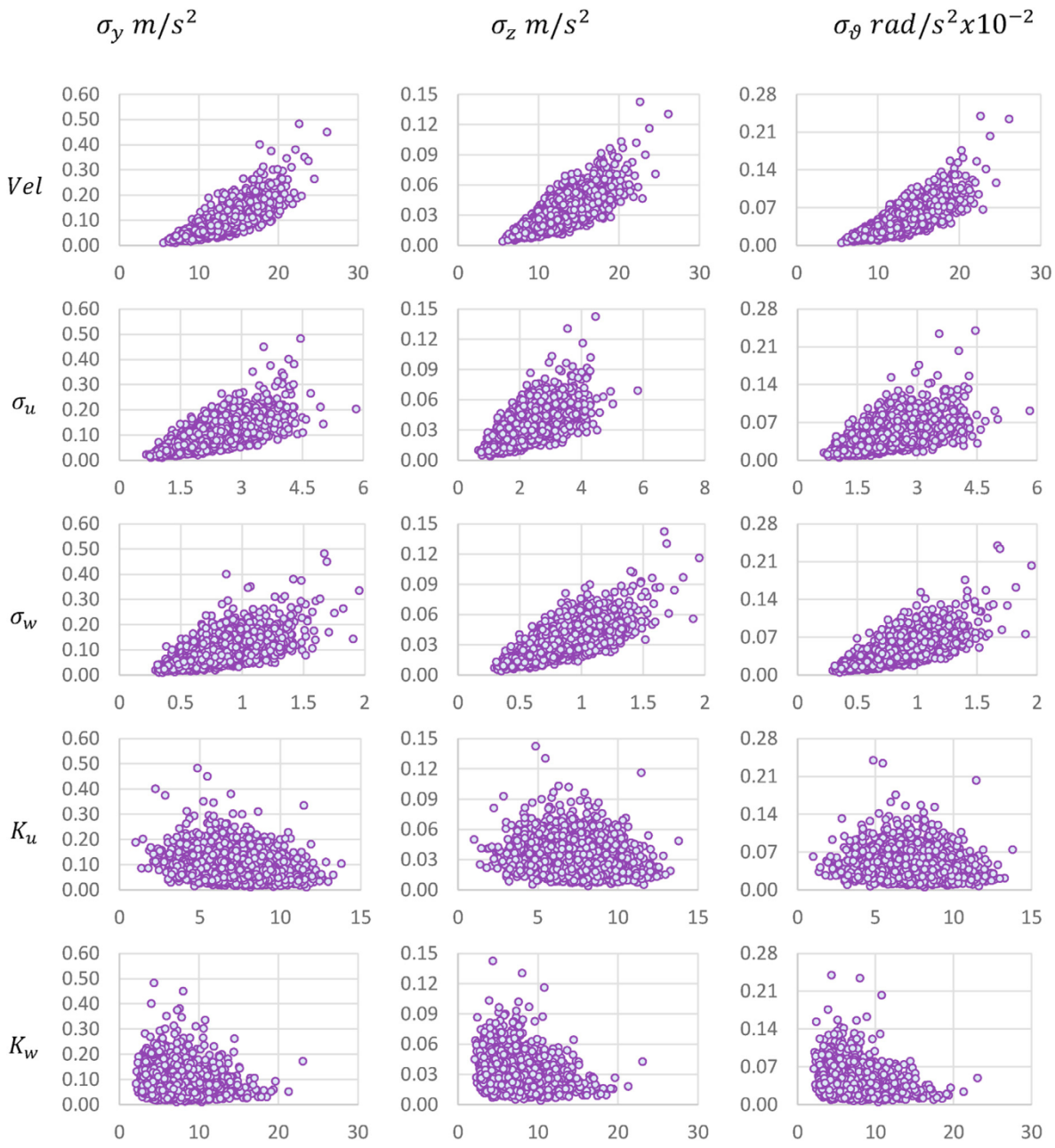

Fig. 8. Random CLHS training dataset (simulated data).

Then, the system's generalized equation of motion is as shown in Equation (14).

$$\begin{aligned} &\tilde{\boldsymbol{M}}_0\,\ddot{\boldsymbol{\eta}}(t) + \left(\tilde{\boldsymbol{C}}_0\right)\dot{\boldsymbol{\eta}}(t) + \left(\tilde{\boldsymbol{K}}_0\right)\boldsymbol{\eta}(t) = \tilde{\boldsymbol{Q}}_{Tot}(t) \\ &\boldsymbol{Q}_{Tot}(t) = \boldsymbol{Q}_{buff}(t) + \boldsymbol{Q}_{se}(t) \end{aligned} \tag{14}$$

Here, $\tilde{\boldsymbol{M}}_0, \tilde{\boldsymbol{C}}_0$ and $\tilde{\boldsymbol{K}}_0$ represent the structural still-air generalized mass, damping and stiffness matrices, respectively, which are diagonal matrices. These structural matrices are obtained from a finite element model of the Hardanger Bridge. Finally, the term $\tilde{\boldsymbol{Q}}_{Tot}$ stands for the total generalized wind load including the buffeting and the self-excited forces.

3.1.2. *Buffeting force using finite element discretization*

Multimodal theory assumes that the structures are line-like. However, suspension bridges have complex shapes; therefore, here, the use of a beam finite element discretization approach is proposed to apply the wind forces in Equation (14). Furthermore, the beam element forces can be transformed into generalized coordinates using the multimodal approach.

A generic structure can be discretized with beam finite elements with 12 degrees of freedom, as shown in Fig. 3 (a). Then, the wind action over a generic beam element is shown in Fig. 3 (b). The three coordinate systems shown in Fig. 3 are the global coordinate system defined by its unit vector $\{E_1, E_2, E_3\}$, the beam element local coordinate system with unit vector $\{e_1, e_2, e_3\}$ and the wind field system with unit vector $\{ev_1, ev_2, ev_3\}$. The transformation scheme from the global coordinate system to the local coordinate system of the beam element is shown in Equation (15) and to the wind field local coordinate system is shown in Equation (16). Hence, Equation (17) shows the transformation from the wind system to the local coordinate system of the beam element.

The vector of nodal buffeting forces is obtained from the principle of virtual work using the shape functions $N(\chi)$ and denoting the wind forces

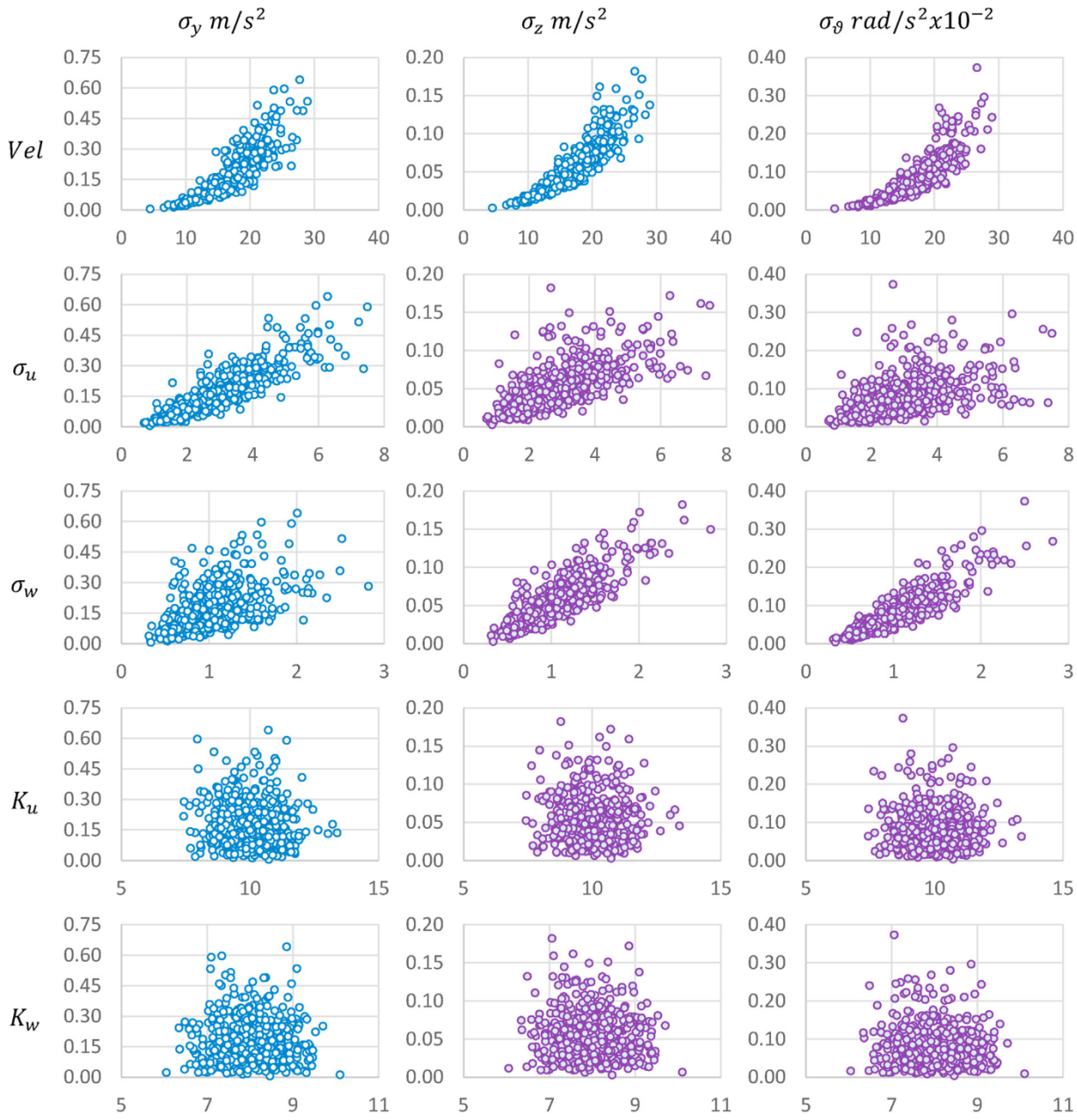

Fig. 9. Testing dataset (simulated data).

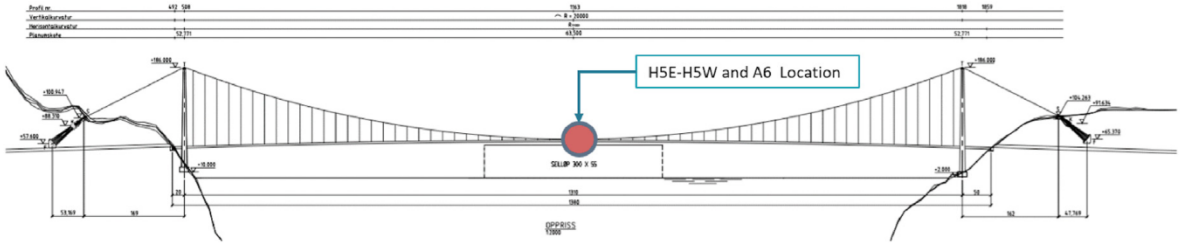

Fig. 10. Hardanger Bridge sensor layout.

in the beam element by $q_{buff}(\chi,t)$ (Equation (18)).

$$\boldsymbol{Q}_{Le\ buff}(t) = \int_0^L \boldsymbol{N}(\chi)\boldsymbol{q}_{buff}(\chi,t)d\chi\ q_{buff}(\chi,t) = \boldsymbol{B}_q(\chi)\boldsymbol{T}_{Lw2Le}\ \boldsymbol{V}_{Lw}(\chi,t) \tag{18}$$

$\boldsymbol{V}_{Lw} = [\,v_1 \quad v_2 \quad v_3\,]^T$ is the vector containing the wind turbulence component in the wind coordinate system, and thus, it shall be transformed into the local coordinate system of the beam. Furthermore, matrix $\boldsymbol{B}_q$can be obtained from Equation (19).

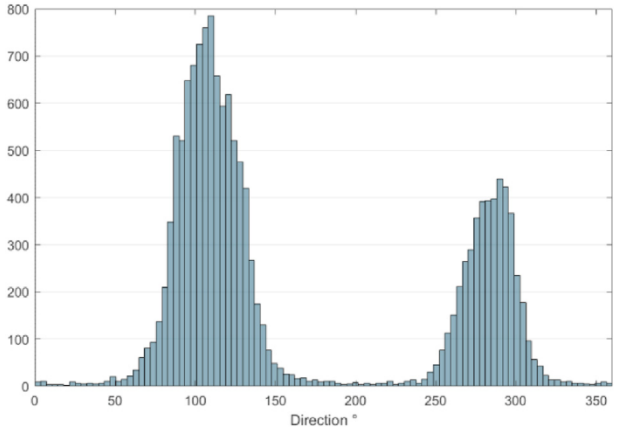

Fig. 11. Histogram of the incoming wind directions from the A6 midspan anemometer of the Hardanger Bridge.

$$\boldsymbol{B}_q(\omega) = \frac{1}{2}\rho B\,\overline{V}\begin{bmatrix} 0 & 0 & 0 \\ 0 & 2\left(\frac{D}{B}\right)\overline{C}_D & \left\{\left(\frac{D}{B}\right)C'_D - \overline{C}_L\right\} \\ 0 & 2\overline{C}_L & \left\{\left(\frac{D}{B}\right)\overline{C}_D + C'_L\right\} \\ 0 & 2B\overline{C}_M & BC'_M \end{bmatrix} \tag{19}$$

where ρ the density of the air, ω the circular frequency, D and B the effective depth and width of the girder cross section, respectively. $\overline{V}$ is the mean wind speed. $\overline{C}_D, \overline{C}_L$ & $\overline{C}_M$ are the drag, lift and moment coefficients at the linearization position from the wind tunnel test and C'_D, C'_L, C'_M are their respective derivates with respect to the angle of attack, these coefficients are given in Table 4 from experimental data and the quantity $\frac{D}{B}$ is introduced as a normalization term.

To assemble the complete vector of nodal buffeting forces, the contribution of all the beam element local forces are transformed into the global coordinate system and summed (Equation (20)). Furthermore, the dependence of $\boldsymbol{B}_q$ and $\boldsymbol{V}_{Lw}$ on the integration variable x is ignored by assuming a uniform shape of the beam elements and that their length is small compared to the spatial variations in the wind field.

$$\boldsymbol{Q}_{buff}(t) = \sum_i^N \boldsymbol{T}_{E2S,i}\,\boldsymbol{T}^T_{G2Le,i} G_i \boldsymbol{B}_{q,i}\boldsymbol{T}_{Lw2Le,i}\,\boldsymbol{V}_{Lw,i}(t) \tag{20}$$

where $\boldsymbol{T}_{E2S}$ is the assembly matrix from the local degrees of freedom of beam element to the global degrees of freedom of the structure and $G_i = \int_0^L \boldsymbol{N}(\chi)d\chi$.

To express the quantities in the frequency domain, the cross-spectral density of the buffeting force is obtained as the discrete Fourier transform of its cross-correlation function

$$R_{\boldsymbol{Q}_{buff}}(\tau) = E\left[\boldsymbol{Q}_{buff}(t)\,\boldsymbol{Q}^T{}_{buff}(t+\tau)\right]\; S_{\boldsymbol{Q}_{buff}}(\omega) = \sum_i^N \times \sum_j^N \boldsymbol{T}_{E2S,i}\,\boldsymbol{T}^T_{G2Le,i} G_i \boldsymbol{B}_{q,i}\boldsymbol{T}_{Lw2Le,i}\,S_V(\Delta x,\omega)\boldsymbol{T}^T_{Lw2Le,j}\,\boldsymbol{B}^T_{q,j}\,\boldsymbol{G}^T_j\,\boldsymbol{T}_{G2Le,j}\boldsymbol{T}^T_{E2S,j} \tag{21}$$

where $S_V(\Delta\chi,\omega)$ represents the cross-power spectral density (CPSD) matrix of the wind field. Then, the cross-spectral density of the buffeting force can be transformed into the generalized coordinate system:

$$\tilde{S}_{\boldsymbol{Q}_{buff}}(\tau) = \boldsymbol{\Phi}(\chi) S_{\boldsymbol{Q}_{buff}}(\omega)\boldsymbol{\Phi}^T(\chi) \tag{22}$$

Applying a similar approach to the self-excited forces, Equation (23) shows the nodal vector of self-excited forces and the wind forces $q_{se}(x,t)$ in the beam element.

$$\boldsymbol{Q}_{Le\,se}(t) = \int_0^L \boldsymbol{N}(\chi)\boldsymbol{q}_{se}(\chi,t)d\chi\; q_{se} = C_{ae}\dot{\boldsymbol{r}}(\chi,t) + K_{ae}\boldsymbol{r}(\chi,t) \tag{23}$$

where C_{ae} *and* K_{ae} are the aeroelastic damping and stiffness matrices, respectively, and are given in Equations (24) and (25). Equations (26) and (27) present the matrices in the generalized coordinate system.

$$C_{ae} = \frac{1}{2}\rho\,\omega B^2\begin{bmatrix} P^*_1 & P^*_5 & BP^*_2 \\ H^*_5 & H^*_1 & BH^*_2 \\ BA^*_5 & BA^*_1 & B^2A^*_2 \end{bmatrix} \tag{24}$$

$$K_{ae} = \frac{1}{2}\rho\,\omega^2 B^2\begin{bmatrix} P^*_4 & P^*_6 & BP^*_3 \\ H^*_6 & H^*_4 & BH^*_3 \\ BA^*_6 & BA^*_4 & B^2A^*_3 \end{bmatrix} \tag{25}$$

$$\tilde{C}_{ae} = \int_L \boldsymbol{\phi}_n^T C_{ae}(\omega^*)\boldsymbol{\phi}_m\,d\chi \tag{26}$$

$$\tilde{K}_{ae} = \int_L \boldsymbol{\phi}_n^T K_{ae}(\omega^*)\boldsymbol{\phi}_m\,d\chi \tag{27}$$

Were $P^*_{1,2,\ldots,6} H^*_{1,2,\ldots,6}$ *and* $A^*_{1,2,\ldots,6}$ Denote the dimensionless aerodynamic derivatives.

Finally, the cross-spectral density of the response in the global Cartesian coordinate system is:

$$S_r(\omega,\chi_r) = \Phi(\chi_r)\left\{\left[H(\omega)S_{\dot{Q}_{buff}}(\omega)\right]H^*(\omega)\right\}\Phi^T(\chi_r) \tag{28}$$

with the following transfer function:

$$H(\omega) = \left[-\tilde{M}_0\omega^2 + \left(\tilde{C}_0 - \tilde{C}_{ae}\right)i\omega + \left(\tilde{K}_0 - \tilde{K}_{ae}\right)\right] \tag{29}$$

By extracting the response spectrum at midspan and integrating over the frequency, it is possible to obtain the standard deviation of the responses and thus the target output features:

$$Y_i = \left[\sigma_y\;\sigma_z\;\sigma_\theta\right]_i = \sigma_r = \int_{-\infty}^{\infty} S_r\left(\omega,\chi_{r\,midspan}\right)d\omega \tag{30}$$

3.1.3. Wind field modeling

3.1.3.1. Cross spectral density function. The cross-spectral density function of the wind turbulent field, $S_V(\Delta\chi,\omega)$, required in Equation (21) is defined as:

$$\boldsymbol{S}_V(\Delta\chi,\boldsymbol{\omega}) = \begin{bmatrix} \boldsymbol{S}_{uu}(\Delta\chi,\boldsymbol{\omega}) & \boldsymbol{S}_{wu}(\Delta\chi,\boldsymbol{\omega}) \\ \boldsymbol{S}_{uw}(\Delta\chi,\boldsymbol{\omega}) & \boldsymbol{S}_{ww}(\Delta\chi,\boldsymbol{\omega}) \end{bmatrix} \tag{31}$$

$$S_{nm}(\Delta\chi,\omega) = Coh_{nm}(\Delta\chi,\omega)\sqrt{S_n(f)S_m(f)} \tag{32}$$

The terms S_n, $n \in \{u,w\}$ and S_m, $m \in \{u,w\}$represent the auto-spectral density function of the turbulence components at an element location x_i. The normalized cospectrum is represented by Coh_{nm}. Furthermore, S_{nm} $n,m \in \{u,w\}$ represents the cross-spectral density function of the beam elements separated by a distance $\Delta\chi$.

The variability of S_V is considered in the wind model parameters. Applied to buffeting response estimation with machine learning, the chosen input features (X) are the incoming mean wind speed (V), the along-wind and vertical turbulence standard deviation (σ_u, σ_w) and the decay coefficients (K_u,K_w). Furthermore, the auto-spectral density is

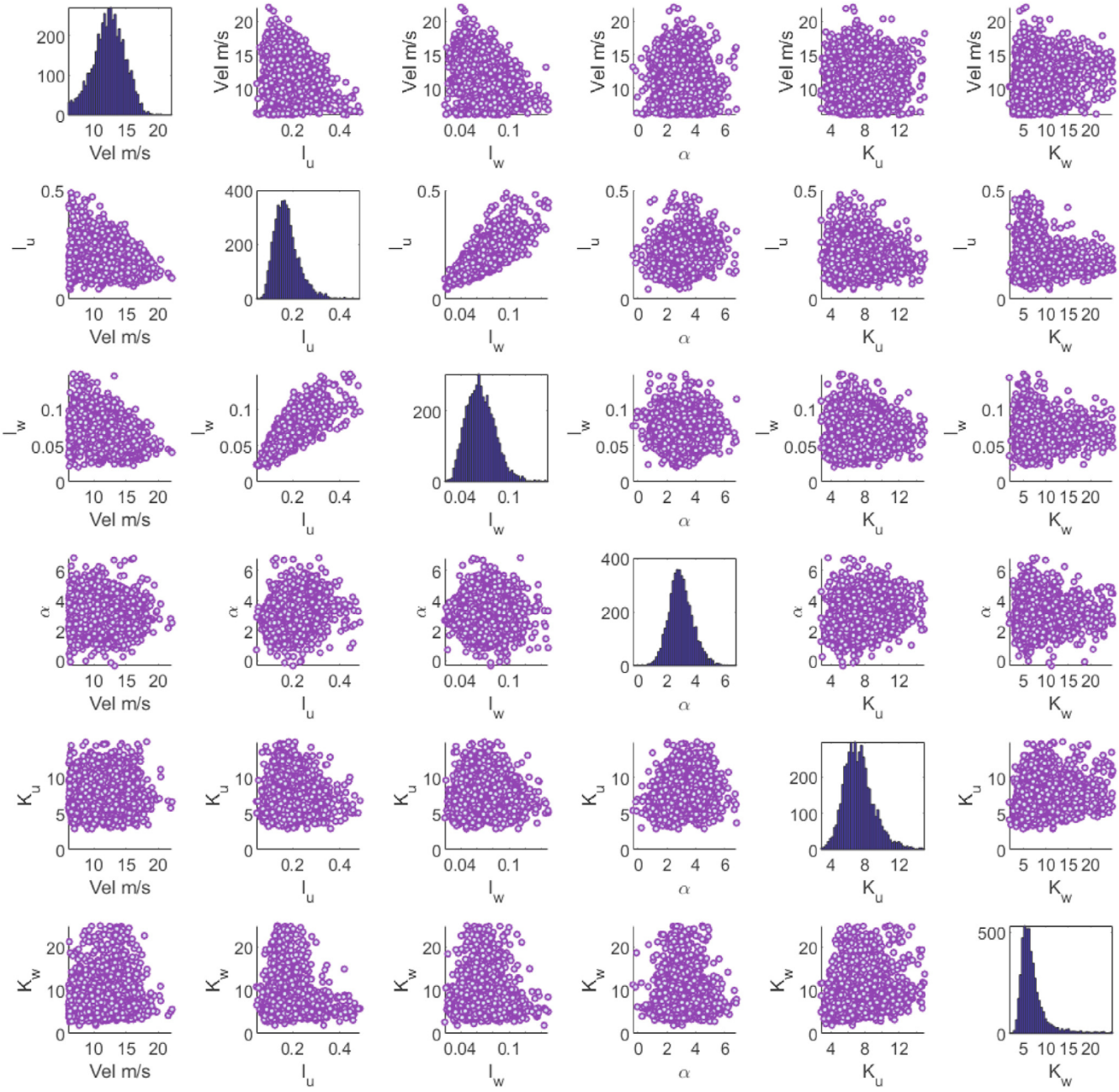

Fig. 12. Matrix plot of the histogram and correlations from the A6 midspan anemometer for the easterly winds dataset.

modeled as a Kaimal-type spectrum (Kaimal et al., 1972) Equation (33), while the normalized co-spectrum is modeled as a Davenport-type (Davenport A. G., 1961) (Equation (34)).

$$\frac{S_n f}{(V\, I_n)^2} = \frac{\mathrm{A}_n f_z}{\left(1 + 1.5\mathrm{A}_n f_z\right)^{5/3}},\ f_z = \frac{z f}{V},\ I_n = \frac{\sigma_n}{V} \tag{33}$$

$$Coh_{nm}(\Delta\chi, \omega) = exp\left(-K_n \frac{\Delta\chi\, f}{V}\right) \tag{34}$$

where the subscripts $n, m \in \{u, w\}$ indicate the along-wind and vertical turbulence components, z is the reference height, f is the frequency and A_n is the set of spectral peak parameters. For the Hardanger Bridge, (Fenerci, 2018) determined that an $A_u$of 30, an A_w of 3 and a z of 60 m are acceptable spectral quantities. I_n represents the turbulence intensities. Furthermore, the cross-coherence and cross-spectral terms associated with Coh_{nm} and S_{nm} when $n \neq m$ are ignored, and thus, only the spatial coherence was considered.

3.2. Synthetic datasets

The corresponding target output (Y) was chosen as the RMS of the lateral, vertical and torsional response components (σ_y, σ_z, σ_θ). Thus, a sample point i in the dataset i represented by the pair X_i, Y_i, as shown in Equation (35).

$$X_i = [V\ \sigma_u\ \sigma_w\ K_u\ K_w]_i \text{ and } Y_i = \left[\sigma_y\ \sigma_z\ \sigma_\theta\right]_i \tag{35}$$

To create the synthetic data using analytical predictions, two training datasets and one testing dataset were created. Each input sample $X_i$contains the wind features applied homogenously to all the wind elements. Furthermore, two different strategies were implemented to simulate the input.

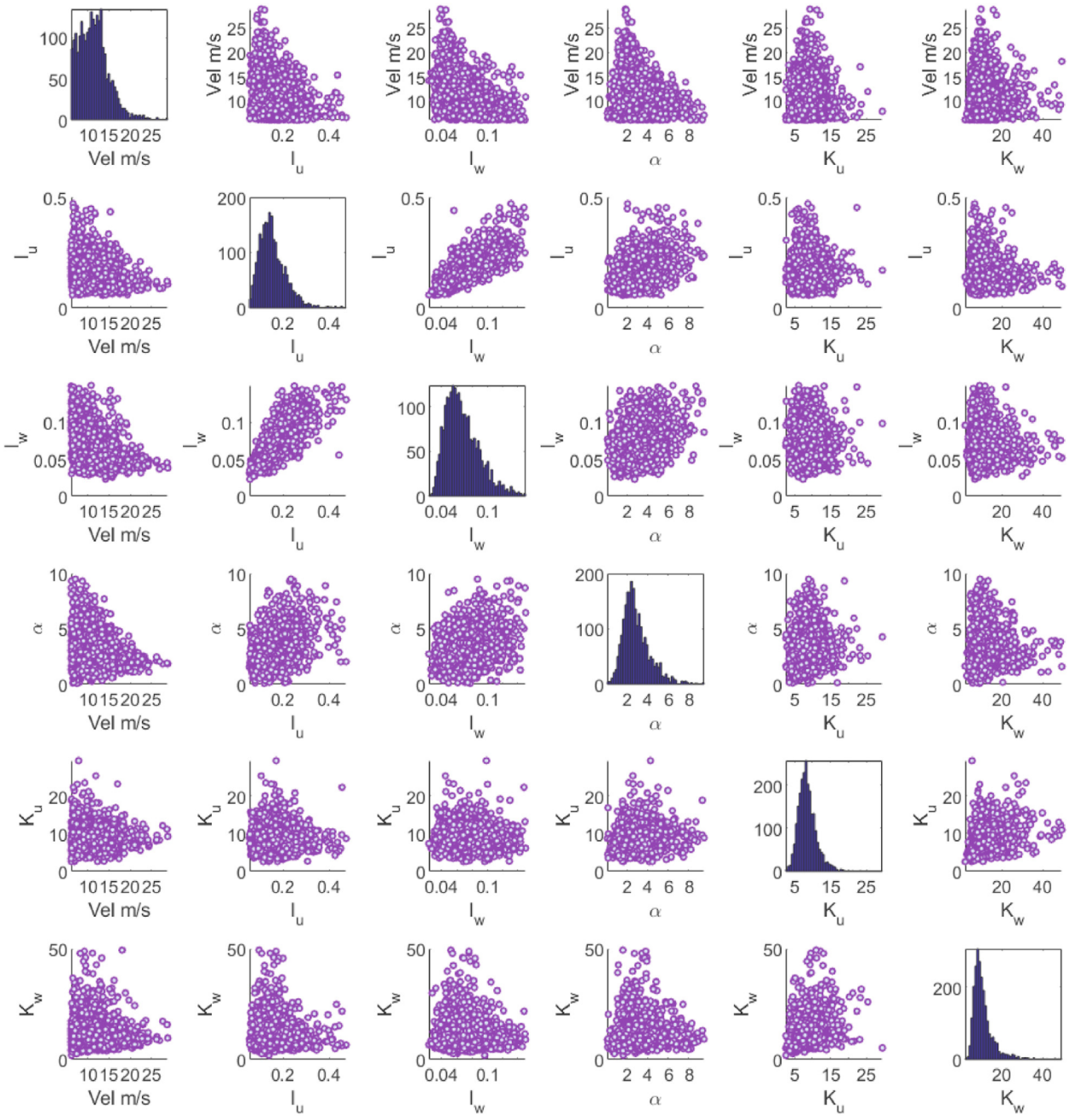

Fig. 13. Matrix plot of histogram and correlations from the A6 midspan anemometer for the westerly winds dataset.

The first strategy is to use a uniform grid of the wind parameters to ensure complete coverage inside the range of the full-scale measurements. Therefore, from the dataset collected by (Fenerci and Øiseth, 2018), the maximum and minimum values bounding each of the wind model parameters were extracted. The resulting discretization range and number of intervals for each variable are reported in Table 1, and with the reported discretization, 25,000 sample points were simulated.

The input from the uniform grid dataset from Table 1 covers the parameter space in a regular manner, which is not the case in the full-scale measurements, where the data are concentrated in certain regions of the parameter space. Therefore, to mimic the real dataset and to investigate how the machine learning algorithms handle such clustering of data points, a second input dataset is generated. This set was created using the extension of the standard Latin hypercube sampling approach (McKay et al., 1979) to correlated variables, correlated Latin hypercube sampling (CLHS) (Olsson et al., 2003). The average size of the directional training datasets to be introduced in the following section is 3500 samples. Therefore, for this dataset, the same number of samples was generated using the CLHS approach following the probability distribution functions and correlation coefficients from the full-scale measurements reported by (Fenerci and Øiseth, 2018).

Finally, following the CLHS generation scheme, a third dataset was generated to test the models. This set allows the validation of the models' generalization ability by examining their performance for the same task. Five hundred samples were generated for this dataset. A summary of the synthetic datasets features is reported in Table 2.

3.2.1. *Analytical prediction of the dynamic response of the Hardanger Bridge*

A schematic technical drawing of the Hardanger bridge's cross section is as shown in Fig. 4. Additionally, the eigenvalue analysis was performed to obtain the still-air modes using a finite element model of the Hardanger Bridge supplied by the Norwegian Public Roads

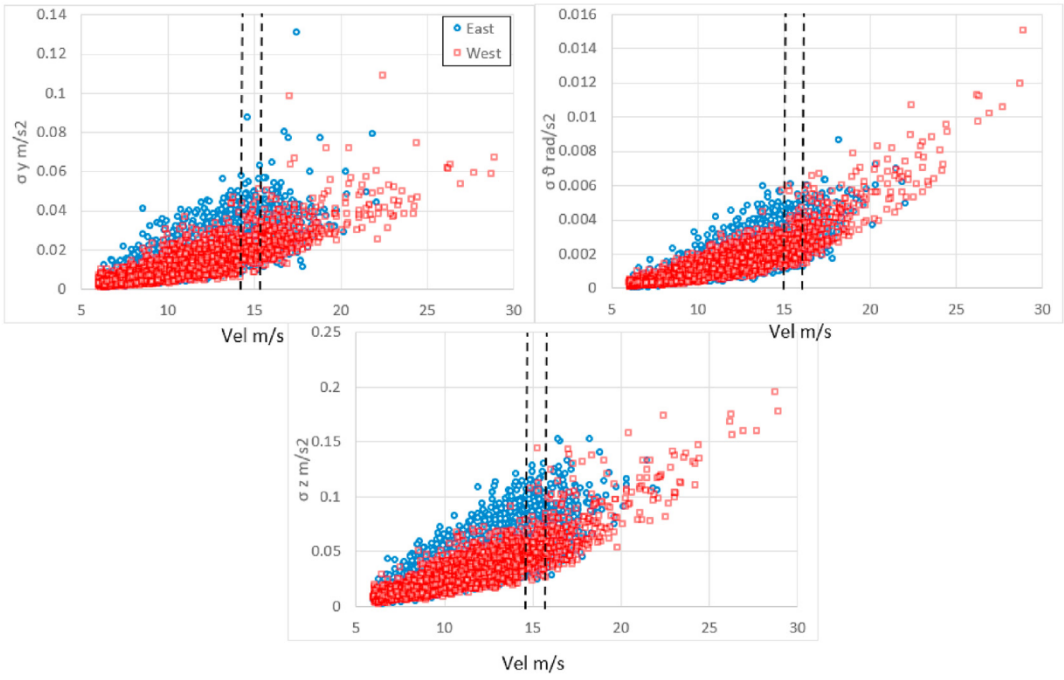

Fig. 14. Training datasets.

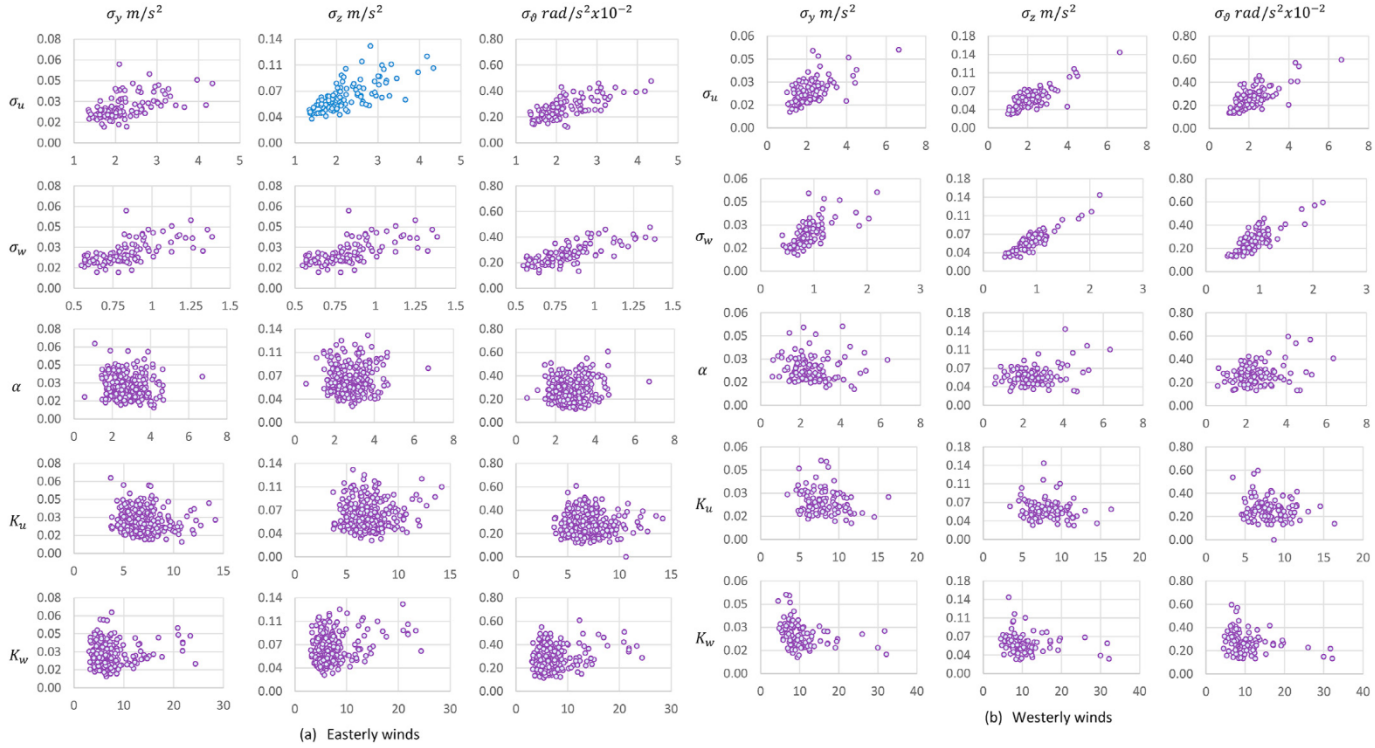

Fig. 15. Training dataset from 15 to 16 m/s a) easterly b) westerly winds.

Administration reported in (Fenerci et al., 2017). Both the girder and cable modal displacements were extracted for this analysis. The first 100 modes were considered in the analysis. The natural frequencies of the first 15 modes are reported in Table 3, the reader is referred to (Fenerci et al., 2017) (Lystad et al., 2020) (Petersen et al., 2017) further details of the bridge's modal behavior. Structural damping was modeled with the Rayleigh damping approach (Chopra, 2000) using the parameters $\alpha_r = 0.0009$ and $\beta_r = 0.01102$. Furthermore, the effective width B and height D of the Hardanger Bridge section are 18.3 and 3.2 m, respectively.

The load coefficients used in the analysis were those reported by (Fenerci and Øiseth, 2018) from wind tunnel testing set up of (Siedziako et al., 2017) and are shown in Table 4. The test was performed with Reynolds number of 2.01×10^5. The scaled cross section of the model was equipped with handrails and the pedestrian path was located upstream.

Additionally (Siedziako et al., 2017), reported the aerodynamic

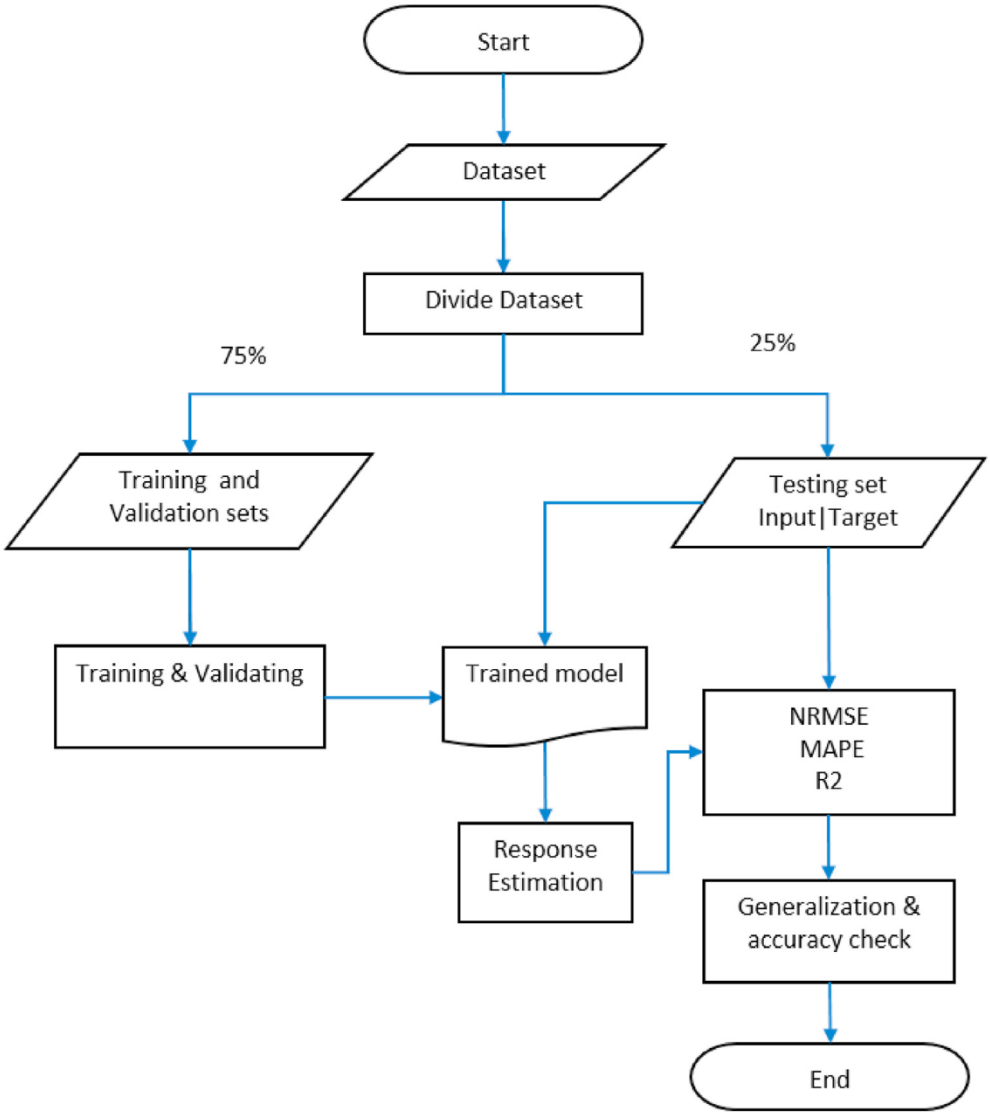

Fig. 16. Flowchart of the model training and comparison steps.

Table 5
ANN settings.

Setting	MLP
Activation function	Rectified linear unit
Cost function	Mean squared error
Optimization	Bayesian-adaptative moment
Number of hidden layers	2
Sizes	8–8
Batch size	10% of the dataset
Learning rate	Min = 1E-7
Number of epochs	1000

Table 6
Grid settings for the SVR hyperparameters.

Setting	Minimum	Maximum	Number of Intervals
Box constraint	1E-5	100	10E14
ε	$1e^{-4}\bar{\varepsilon}$	$1e^{2}\bar{\varepsilon}$	10E14
Polynomial degree	3	6	3

derivatives of the bridge cross section from the wind tunnel test. Fig. 5 and Fig. 6 show the experimental results of the 18 aerodynamic derivatives fitted a polynomial function that tends constant values outside the experimental data range. In the figures the reduced frequency $K = \frac{\omega B}{V}$ is introduced in the notation to enhance the presentation of the aerodynamic derivatives. Nonetheless, for the purposes of the surrogate modelling with synthetic datasets the use of the quasi steady theory showed to be sufficient. Therefore, the aerodynamic derivatives formulation was used just for the full-scaled measurements.

Finally, using the three simulated wind inputs described in the previous section (two inputs are used for training, one input is used for testing), the dynamic response of the Hardanger Bridge, namely, the RMS of the lateral, vertical and torsional components, was obtained using multimodal buffeting theory. The scatter plots showing the resulting input-output relationships are shown in Figs. 7-9 for the training uniform, training CLHS and testing CLHS datasets, respectevely.

3.3. Full-scale measurement data from the Hardanger Bridge

3.3.1. Overview of the measurements

The buffeting responses of the Hardanger Bridge were measured with an extensive measurement system composed of 9 ultrasonic anemometers that measure the wind speed in the range from 0 to 65 m/s with a 0.001 m/s resolution at a 32 Hz sampling frequency and 20 triaxial accelerographs that measure accelerations on the interval of ±4*g* at a

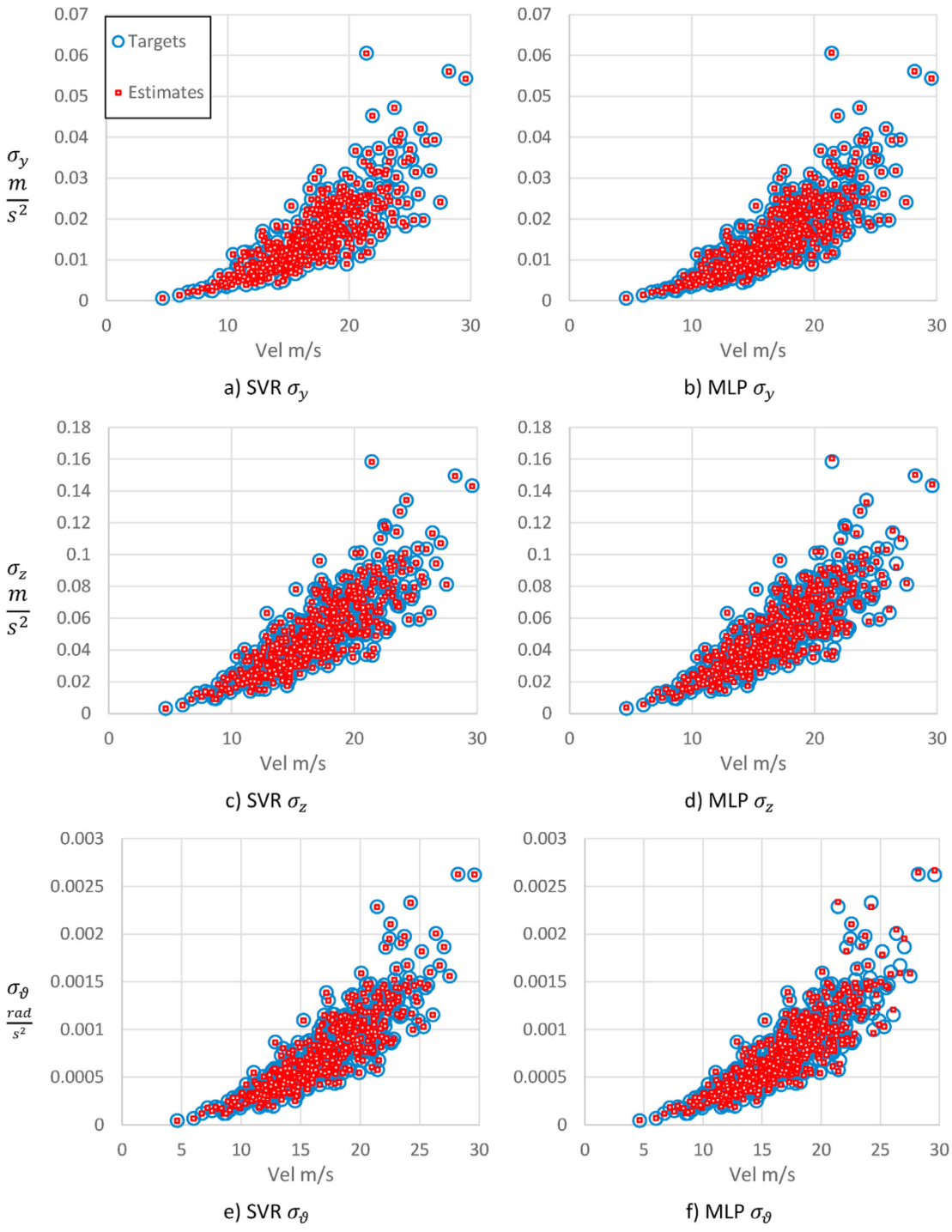

Fig. 17. Response panel plot for models trained with a uniform grid dataset for the (a) SVR σ_y (b) MLP σ_y (c) SVR σ_z (d) MLP σ_z (e) SVR σ_ϑ (f) MLP $\sigma_\vartheta$models.

200 Hz sampling frequency. More details on the Hardanger Bridge measurement system and dataset management procedure are given in (Fenerci, 2018), the dataset is available in open access (https://doi.org/10.21400/5ng8980s) (Fenerci et al., 2018). The installed anemometers record the incoming wind velocity in polar coordinates, while the coupled arrangement of the accelerometers register the triaxial bridge response (Fenerci et al., 2017).

3.3.2. *Wind field modeling and turbulence parameters*

The wind parameters were extracted from the measurement system at the A6 anemometer location (Fig. 10). Previous research campaigns at the site (Fenerci and Øiseth, 2018) (Fenerci et al., 2017) (Lystad et al., 2018) reported two data clusters in the mean wind direction histogram (Fig. 11). This phenomenon poses a challenge to the analysis due to the topography-related difference between the wind features depending on the incoming wind direction (Fenerci et al., 2017). Thus, in a similar manner as the previous campaigns, the WIVs from both clusters were studied separately.

Fig. 12 and Fig. 13 show the wind parameter matrix plots for the easterly and westerly wind datasets; the subfigures on the diagonal contain each input variable histogram, and the figures on the off-diagonal show the scatter plots between the parameters. Furthermore, the angle of attack, α, is introduced as an input parameter for this case, unlike the synthetic data.

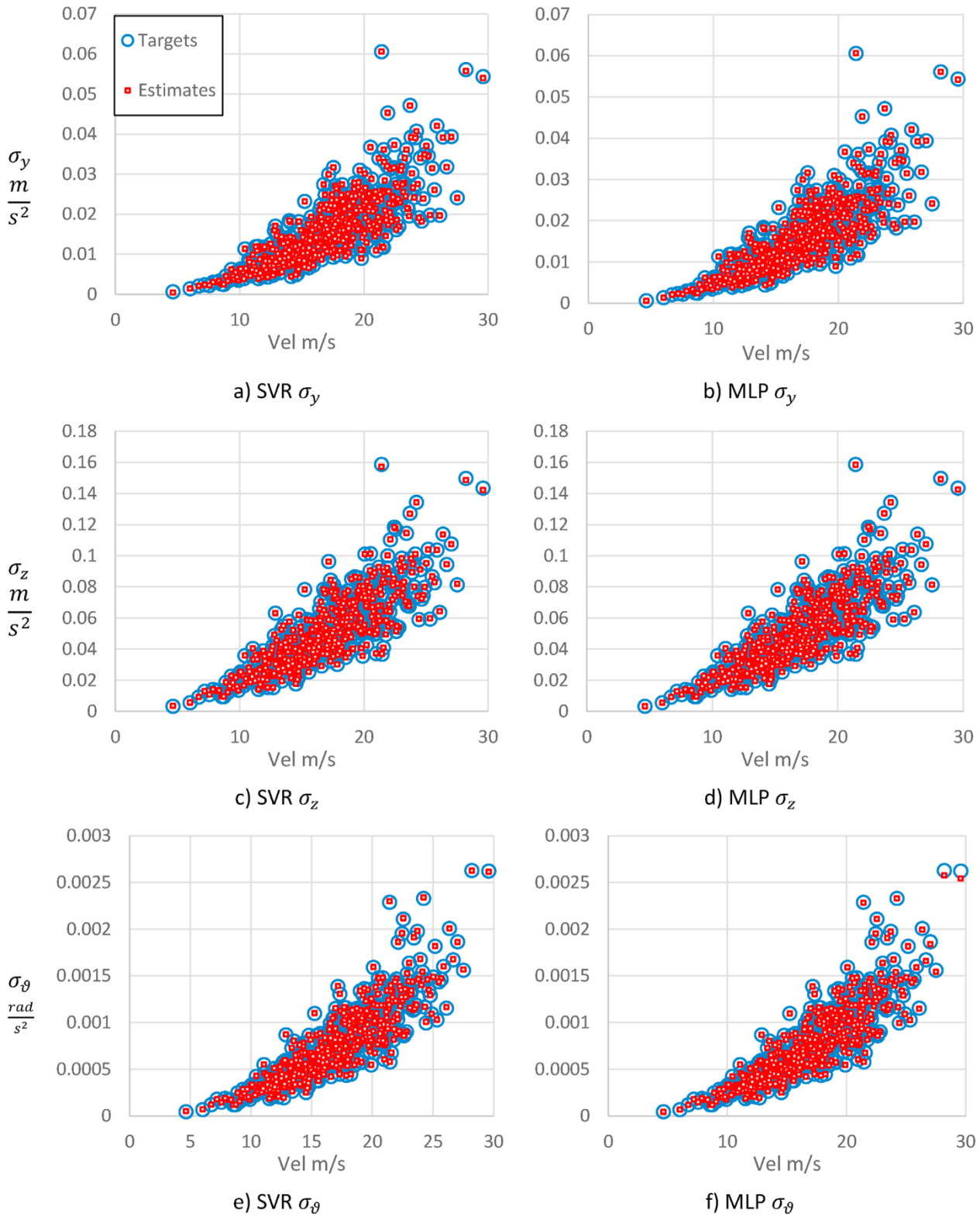

Fig. 18. Response scatter plot comparison for the models trained with the CLHS dataset for the (a) SVR σ_y (b) MLP σ_y (c) SVR σ_z (d) MLP σ_z (e) SVR σ_ϑ (f) MLP $\sigma_\vartheta$models.

3.3.3. Root mean square (RMS) of the responses at the midspan

The response of the Hardanger Bridge was measured at the same location as the wind input using the accelerometer coupled sensors H5 shown in Fig. 10. The lateral and vertical components of the acceleration were obtained as the average from the sensors at both sides of the girder, while the torsional component was computed by dividing the difference between the two vertical signals by their distance (13 m). Fig. 14 shows the panel plots of the training datasets for the westerly and easterly winds. These plots contain the structural responses at the midspan of Hardanger Bridge from the accelerometer coupled sensors H5 as described in (Fenerci et al., 2017). The figures show quadratic trends between the velocities and the responses, as expected. Fig. 15, on the

Table 7
Comparison of the evaluation metrics on the simulated datasets.

Model		NRMSE			MAPE			R2		
		σ_y	σ_z	σ_θ	σ_y	σ_z	σ_θ	σ_y	σ_z	σ_θ
Uniform grid	MLP	1.02E-03	5.87E-03	7.21E-03	0.4751	1.7468	1.936	1.00	0.99	0.99
Uniform grid	SVR	5.14E-04	1.66E-03	7.70E-04	0.1853	0.5748	0.303	1.00	1.00	1.00
Random CLHS	MLP	1.46E-04	3.51E-04	1.76E-03	0.0092	0.0120	0.036	1.00	1.00	1.00
Random CLHS	SVR	4.97E-04	8.90E-04	6.62E-04	0.1465	0.1233	0.115	1.00	1.00	1.00

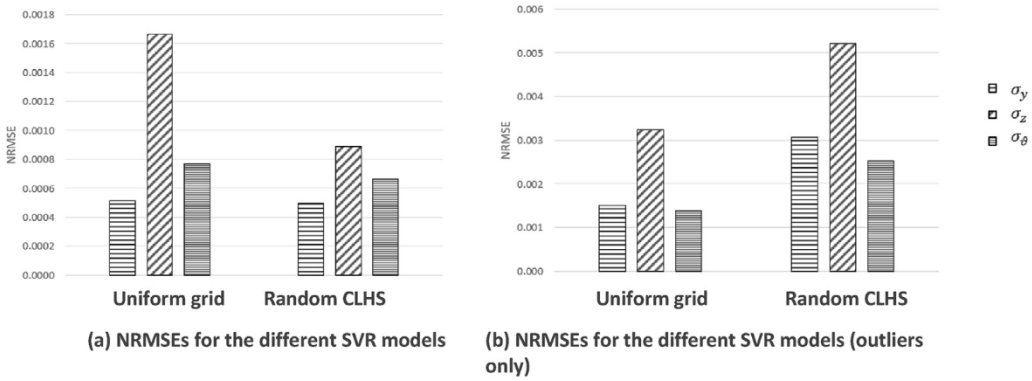

Fig. 19. (a) NRMSEs for the different SVR models (b) NRMSEs for the different SVR models (outliers only).

other hand, shows the variation in the structural responses as a function of the complementary wind input parameters for the velocity range from 15 to 16 m/s of the a) easterly and b) westerly winds. This figure shows linear trends between the responses and the turbulence intensities, and no apparent trend can be observed for the other parameters.

4. Training, validation and testing datasets

The training datasets correspond to the division of the data that will be fed into the machine learning models; for this type of application, it is deemed appropriate to take 65% of the dataset for training. Furthermore, 10% of the dataset was used as a validation dataset for tuning the model hyperparameters and optimizing the global performance. Thus, an additional 25% remained for the testing data. The schematic flowchart of the analysis is shown in Fig. 16.

4.1. Model hyperparameters and settings

In ANN models, the network architecture, function selection and optimization scheme affect the results. Thus, Equation (5) minimizes the loss function for a given network setting. With the aim of avoiding overtraining, the MLP model was trained using the batch training strategy; i.e., every optimization cycle was performed on a different division of the dataset. The configuration found to be appropriate for training the MLP models is reported in Table 5.

Analogously, for the SVR model, Equation (12) will give rise to different estimation functions if changes are made to the kernel function, box constraint C, and slack parameters ξ, among other settings. For this application, experience suggests the use of a polynomial function as the kernel function, as given in Equation (36), and half the width of the ε-insensitive band, $\bar{\varepsilon}$, is computed by Equation (37). Then, a built-in grid search optimization algorithm is used to find the configuration that minimizes the loss functions with the grid setting reported in Table 6. Further studies on hyperparameter optimization for buffeting response modeling are beyond the scope of this paper but may be the objective of future research.

$$K(x_i' x) = \left(1 + x_i' x_j\right)^d \tag{36}$$

$$\bar{\varepsilon} = \frac{interquartile\ \{range(\mathbf{y})\}}{13.49} \tag{37}$$

5. Performance assessment and comparison

5.1. Performance metrics

Three metrics were used to compare the estimates and targets: the normalized root mean square error (NRMSE, Equation (38)) (Amstrong and Collopy, 1992), the mean absolute percent error (MAPE, Equation (39)) and the coefficient of determination (R2, Equation (40)). The NRMSE (Amstrong and Collopy, 1992) becomes representative of the modeling since it is the normalized version of the square root of the mean squared error (MSE), which is used as the loss function for the MLP. On the other hand, the MAPE results are more intuitive since they present the deviation as a percent. Finally, R2 allows the weight of the deviation of the estimates according to their variance.

$$NRMSE = \sqrt{\frac{1}{N}\sum_{j=1}^{N}\left(\hat{y}_j - y_j\right)^2} \Big/ \{max(Y) - \min(Y)\} \tag{38}$$

$$MAPE = \frac{1}{N}\sum_{j=1}^{N}\frac{\left|\hat{y}_j - y_j\right|}{y_j} \tag{39}$$

$$R2 = 1 - \sum_{j=1}^{N}\left(\hat{y}_j - y_j\right)^2 \Big/ \left(y_j - \bar{y}\right)^2 \tag{40}$$

5.2. Synthetic data

5.2.1. Uniform grid training dataset

The panels in Fig. 17 show the comparison between the targets from the testing dataset and estimates for the machine learning models trained with the linearly spaced dataset for the SVR response models and for the MLP. In the figure, the X-axis is the velocity, and the Y-axis is the RMS of the response component. The figures show a complete matching of the estimation and target over the entire wind speed range. The satisfactory

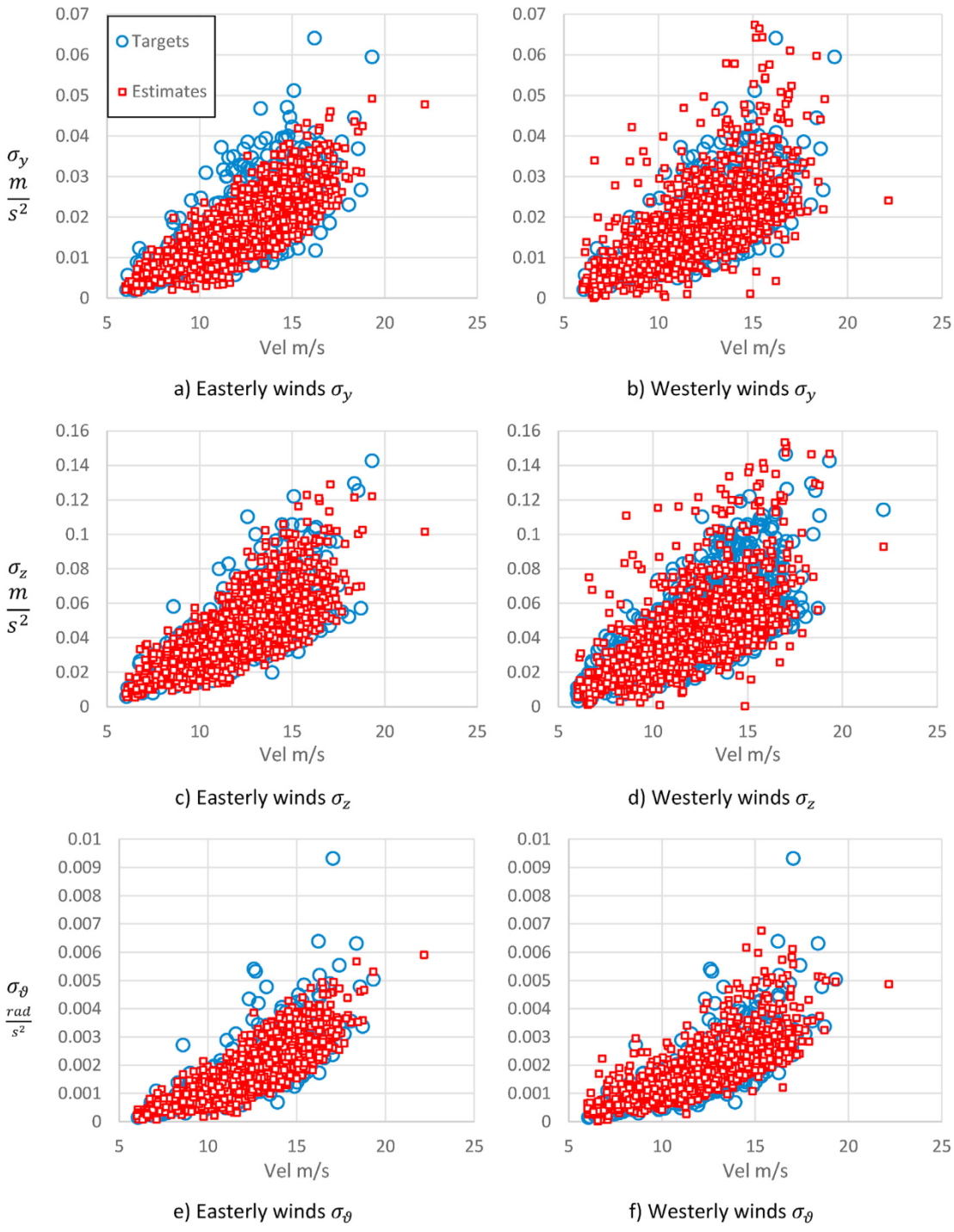

Fig. 20. Response comparisons SVR models (a) Easterly $\boldsymbol{\sigma_y}$ (b) Westerly $\boldsymbol{\sigma_y}$ (c) Easterly $\boldsymbol{\sigma_z}$ (d) Westerly $\boldsymbol{\sigma_z}$ (e) Easterly $\boldsymbol{\sigma_\vartheta}$ (f) Westerly.$\boldsymbol{\sigma_\vartheta}$

performance of the machine learning models on the simulated dataset shows the effectiveness of the method in modeling the buffeting phenomenon and encourages its application to the full-scale data.

5.2.2. Random training dataset

Analogously, the comparison of the scatter plots between the randomly generated dataset target from the testing dataset and its corresponding machine learning estimates is shown in Fig. 18. Despite the clustering of the data points around the moderate wind speeds, the algorithm is successful in predicting the response in the entire wind speed range.

Table 7 extends the graphical overview and reports the evaluation metrics of the three response components (i.e., σ_y, σ_z and σ_ϑ) for the two machine learning models (i.e., the MLP and SVR models) on the two different datasets (i.e., the uniform grid and random CLHS datasets). With the given evaluation metrics, the SVR models perform better than MLP models in the uniform grid dataset, whereas the opposite occurs in the random CLHS dataset. Nevertheless, the order of magnitude of the NRMSE is approximately 10E-4, stating an appreciably good general performance level, with the lowest error of 1.46E-04 for the MLP/CLHS/σ_y response and the highest of 7.21E-03 in MLP/uniform grid/σ_ϑ. Moreover, the highest and lowest MAPE values of 1.936% and 0.0092% agree with the NRMSE results.

Estimation of extreme responses is especially important for long-span

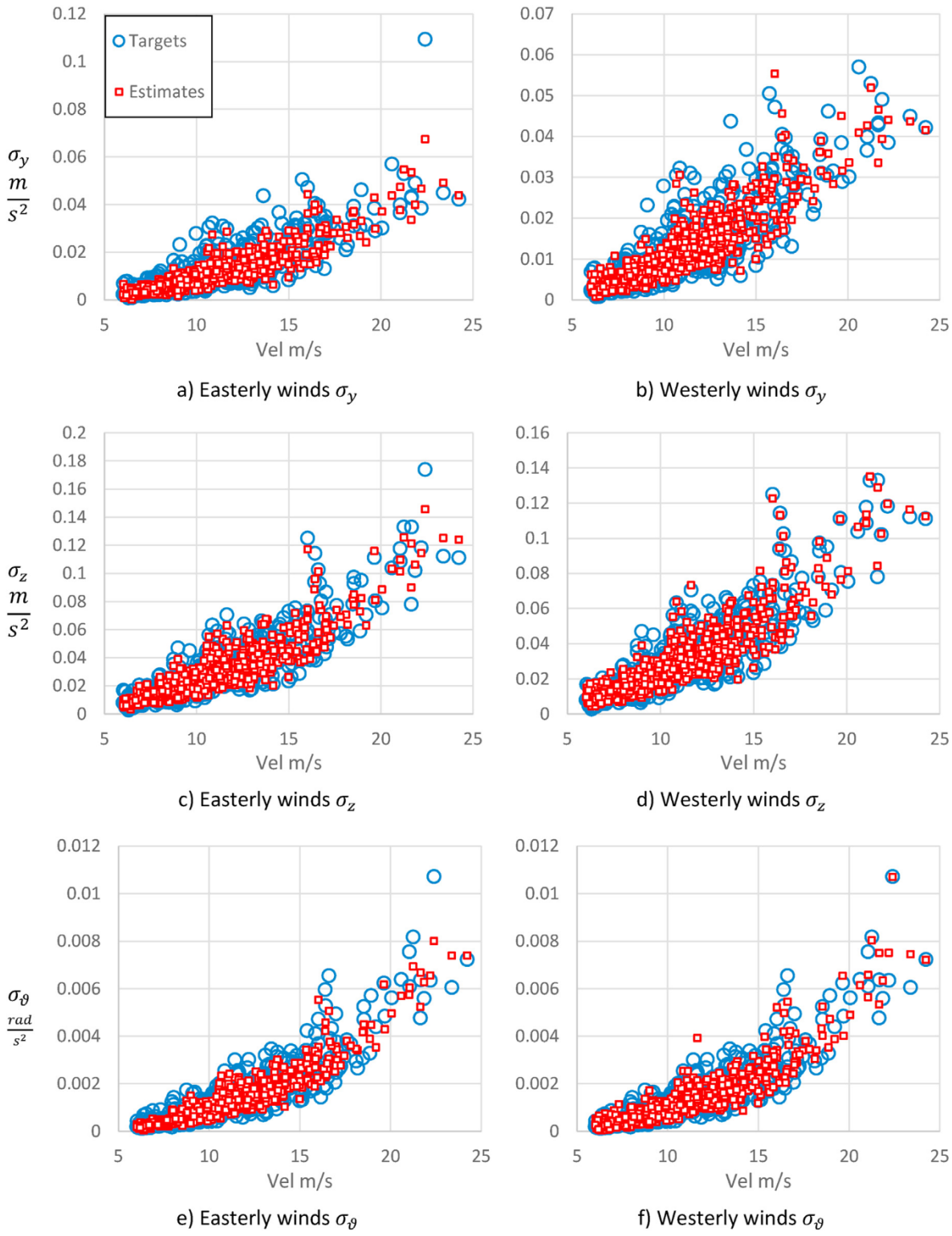

Fig. 21. Response comparisons MLP models (a) Easterly σ_y (b) Westerly σ_y (c) Easterly σ_z (d) Westerly σ_z (e) Easterly σ_ϑ (f) Westerly.σ_ϑ

bridge buffeting response modeling. Thus, a comparison limited to the maximum values given by $\sigma_y > 0.3$, $\sigma_z > 0.1$ and $\sigma_\vartheta > 0.018$ is presented. To highlight the difference in the performance, Fig. 19 (a) reports the NRMSE of the SVR models in the general case and (b) reports the maximum values. Overall, the models trained with the random CLHS dataset showed less error compared to their uniform grid counterparts. However, for the outliers, the uniform grid models performed better because the CLHS dataset concentrates the data points in the central region, leaving fewer data points in the maximum value region, resulting in better predictions for moderate wind speeds and compromising the accuracy of the extreme values. On the other hand, the uniform grid dataset presents a better accuracy in the region of the outliers. It should be noted that both methods provide reasonably accurate results.

Table 8
Evaluation metrics for the directional models on real datasets.

Model	NRMSE			MAPE			R2		
	σ_y	σ_z	σ_ϑ	σ_y	σ_z	σ_ϑ	σ_y	σ_z	σ_ϑ
West MLP	6.87E-02	5.39E-02	3.79E-02	26.8	10.7	19.5	0.89	0.95	0.92
West SVR	5.14E-02	3.06E-02	3.28E-02	21.6	14.1	22.2	0.84	0.94	0.92
East MLP	8.87E-02	1.06E-01	5.74E-02	42.0	36.4	29.1	0.44	0.59	0.72
East SVR	5.98E-02	5.65E-02	4.87E-02	22.9	13.9	19.4	0.69	0.84	0.80

Table 9
Constant input values for the directional model comparisons.

Wind feature	Symbol	Constant value
Along-turbulence SD	σ_u	$0.1*V$
Vertical turbulence SD	σ_w	0.06*V
Angle of attack	α	2.9
Along-wind decay coefficient	K_u	8.6
Vertical decay coefficient	K_w	10.7

5.3. Full-scale measurement data

The techniques verified with the synthetic data case were extended to full-scale measurements. For this aim, the scatter plots the response comparisons from the different models are shown in Figs. 20 and 21. Additionally, Table 8 shows the evaluation of the three response components (σ_y, σ_z and σ_ϑ) for the two machine learning models (MLP and SVR) in the two different datasets (westerly and easterly winds).

The easterly and westerly wind model estimates were compared. The input was varying mean wind speeds, with linearly dependent σ_u,σ_w (to retain the observed trend in the real data), and the other parameters were held constant. Table 9 reports the input parameter settings. Fig. 22 shows the plots comparing the predictions of both directional models for the three response components σ_y, σ_z and σ_ϑ from the SVR algorithm, while Fig. 23 reports a similar comparison for the MLP model.

Both figures show that the model trained with the easterly wind dataset yields a higher response estimation for the same input conditions. This is consistent with the behavior observed in the full-scale measurements reported in Fig. 14.

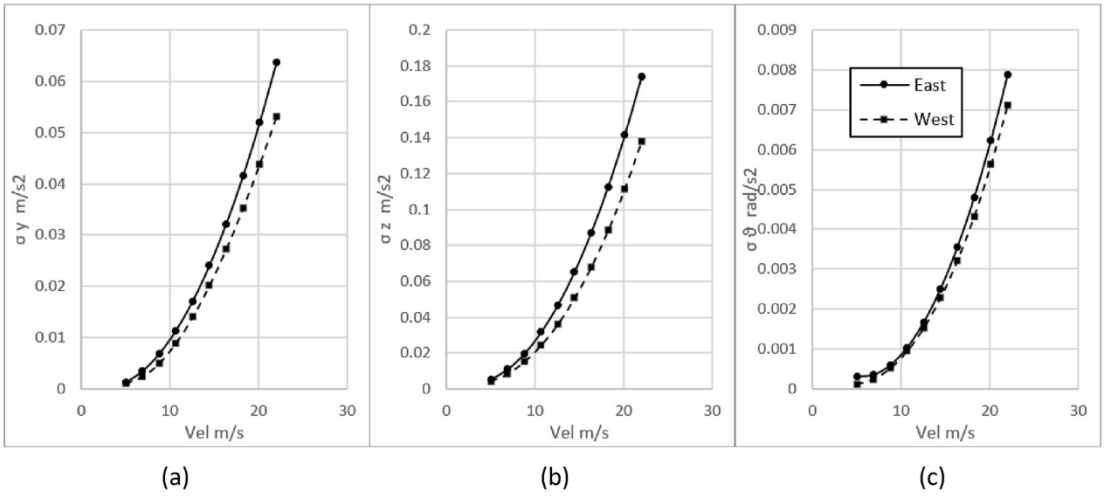

Fig. 22. Prediction comparison for the directional SVR models on common input: (a) σ_y, (b) σ_z and (c).σ_ϑ

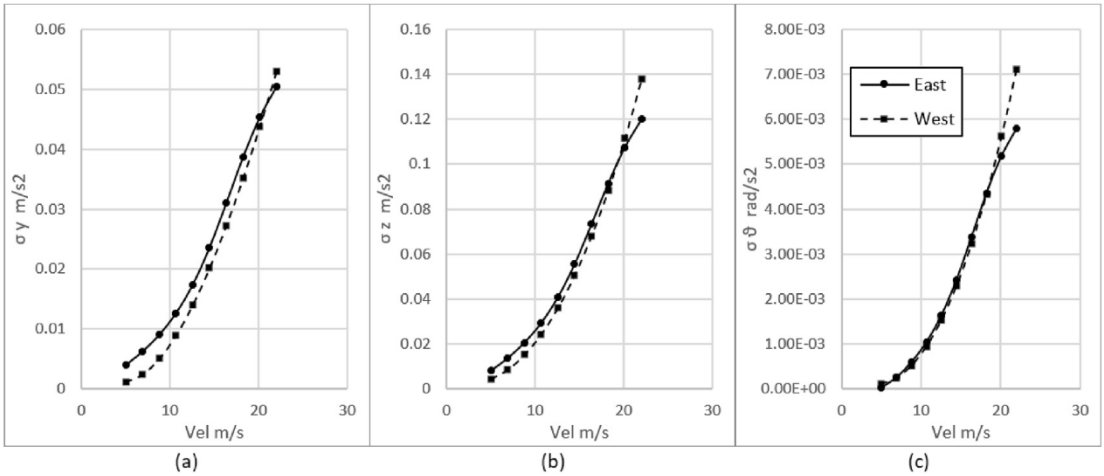

Fig. 23. Prediction comparison for the directional MLP models on common input: (a) σ_y, (b) σ_z and (c).σ_ϑ

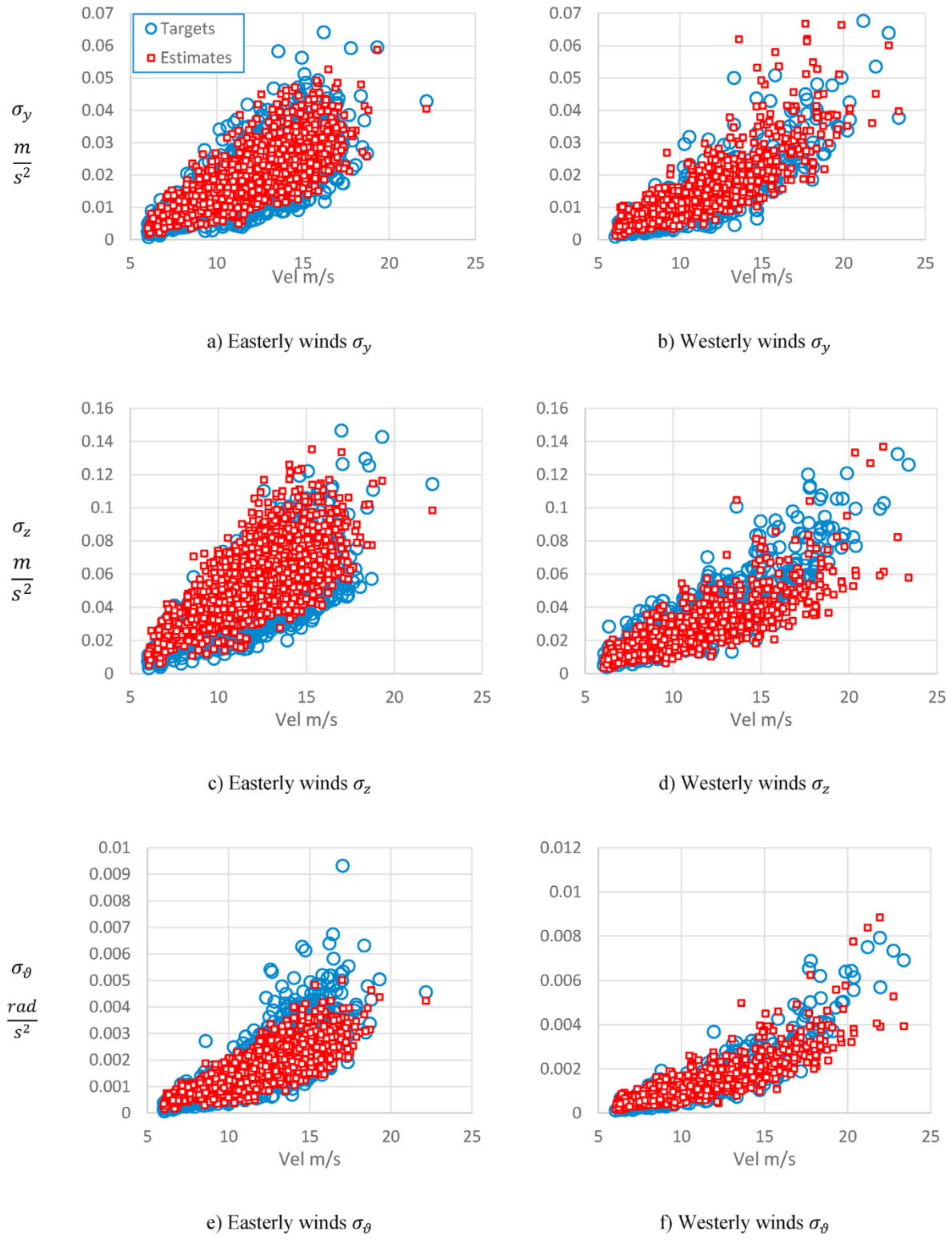

Fig. 24. Response comparison computed with buffeting theory (a) Easterly σ_y (b) Westerly σ_y (c) Easterly σ_z (d) Westerly σ_z (e) Easterly σ_ϑ (f) Westerly.σ_ϑ

Table 10
Evaluation metrics for the estimates from buffeting theory.

Model	NRMSE			MAPE			R2		
	σ_y	σ_z	σ_ϑ	σ_y	σ_z	σ_ϑ	σ_y	σ_z	σ_ϑ
West BFT	7.65E-02	6.27E-02	5.47E-02	38.68	19.13	34.17	0.82	0.85	0.83
East BFT	7.62E-02	1.12E-01	5.97E-02	33.58	35.41	24.81	0.54	0.73	0.72

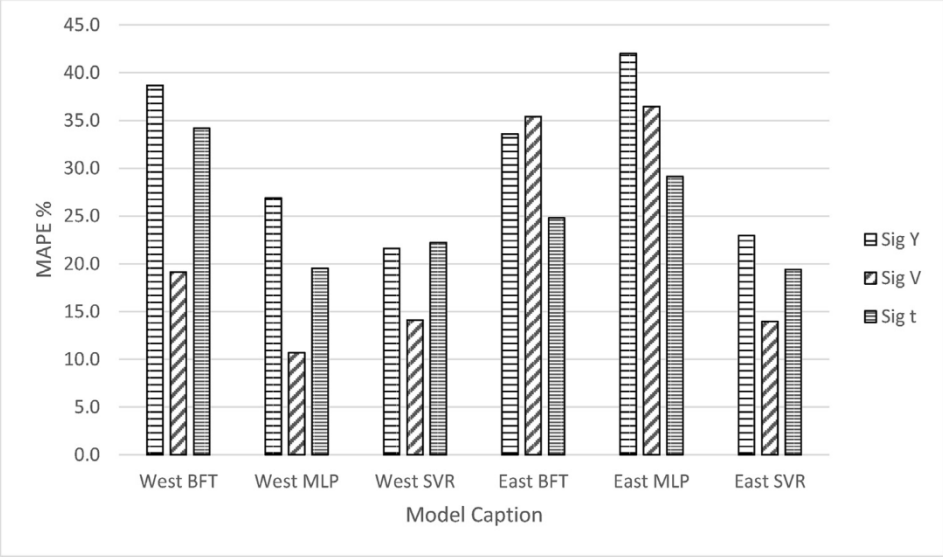

Fig. 25. MAPEs computed with buffeting theory and machine learning.

5.4. *Machine learning vs. buffeting theory*

Finally, the response of the Hardanger Bridge was estimated analytically using buffeting theory and the wind input from the full-scale measurements. The response comparison between the measured response and the buffeting theory estimation is shown in Fig. 24, and the corresponding evaluation metrics are reported in Table 10. A graphical comparison in terms of the MAPE between the estimates obtained with machine learning reported in Table 8 and the estimates obtained with buffeting theory is shown in Fig. 25.

The SVR estimates yield more accurate results than the MLP and buffeting theory on both directional datasets. Moreover, for the westerly winds dataset, both machine learning models predicted more accurate estimate than buffeting theory. Using the MAPE, the greater difference between buffeting theory and the SVR model was 17% for σ_y and the lowest difference was approximately 5% for σ_z on the easterly winds' dataset. In general, the estimates of the full-scale observations show a slight decrease in the performance compared with the ideal case, mainly because uncertainties in the dynamic behavior, such as the inhomogeneities and non-stationarity of the wind field, traffic and temperature effects are not completely captured by analytical models.

A difference in the error metrics between easterly and westerly wind related responses is exposed for both cases, estimations with machine learning (Table 8) and buffeting theory estimation (Table 10). For example, R2 metrics for the σ_y responses in Table 8 vary from 0.44 (easterly) to 0.89 (westerly) for MLP and 0.69 (easterly) to 0.84 (westerly) for SVR whereas Table 10 shows a variation from 0.54 (easterly) to 0.82 (westerly) for the same response component. The main reason for this behavior is that the aerodynamic properties of the bridge, namely the steady-state force coefficients (Table 4) and the aerodynamic derivatives (Figs. 5–6) were obtained for the case of winds approaching from the west, which are the strongest. This partly explains the poor performance of the analytical predictions for the easterly winds. Further, the easterly winds are more affected by the more complex topography, which typically causes higher angles of attack. Such issues are handled implicitly by the machine learning models, where the buffeting theory is more challenging.

6. Conclusion

In this paper, accurate buffeting response estimations were computed from analytical and machine learning models. The wind input dataset was obtained from full-scale measurements and simulated data following the probabilistic model of the observed wind turbulence field. Then, the quality of the estimates was evaluated, leading to the following conclusions:

- Estimations from machine learning models (i.e., the SVR and MLP models) on the synthetic datasets were reasonably accurate. Therefore, the good quality of the estimates makes the technique suitable for surrogate model development such as those required in reliability analyses.
- The models trained with the full-scale datasets were less accurate than the models trained with the synthetic datasets. The main reasons for this are the various uncertainties in the dynamic behavior that are not captured by the monitoring system, such as the inhomogeneities and non-stationarity of the wind field, traffic and temperature effects. However, as data-driven models bypass some of the limitations of buffeting theory, machine learning-based estimates were more accurate than the analytical predictions.
- Considering the slightly different behavior observed under easterly and westerly winds, two different machine learning models were trained for the two directions. The models trained on the easterly winds predicted higher responses under the same wind input, capturing the observed behavior.
- The SVR model yielded better response predictions than the MLP model on both the simulated and full-scale measurements. Furthermore, the method was more accurate that the analytical response estimates with the multimodal approach.

CRediT authorship contribution statement

Dario Fernandez Castellon: Writing - original draft, Software, Methodology, Formal analysis. **Aksel Fenerci:** Writing - review & editing, Data curation, Investigation. **Ole Øiseth:** Conceptualization, Supervision, Project administration.

Declaration of competing interest

The authors declare that they have no known competing financial interests or personal relationships that could have appeared to influence the work reported in this paper.

Acknowledgements

The research presented in this paper was financially supported by the Norwegian Public Roads Administration (Statens Vegvesen) as a part of the E-39 coastal highway project.

References

Fenerci, A., Øiseth, O., 2018. Site-specific data-driven probabilistic wind field modelling for wind-induced response prediction of cable-supported bridges. J. Wind Eng. Ind. Aerod. 181, 161–179.
Alpaydin, E., 2020. Introduction to Machine Learning, fourth ed. Massachusetts Institute of Technology, Cambridge, Massachusetts.
Amstrong, J.S., Collopy, F., 1992. Error measures for generalizing about forecasting. Int. J. Forecast. 8 (1), 69–80.
Awad, M., Khanna, R., 2015. Support vector regression. In: Efficient Learning Machines. apress, Berkeley, CA.
Bernardini, E., Spence, S.M., Wei, D., Kareem, A., 2015. Aerodynamic shape optimization of civil structures: a CFD-enabled Kriging-based approach. J. Wind Eng. Ind. Aerod. 144, 154–164.
Bietry, J., Delaunay, D., Conti, E., 1995. Comparison of full-scale measurement and computation of wind effects on a cable-stayed bridge. J. Wind Eng. Ind. Aerod. 57 (2–3), 225–235.
Bishop, C.M., 1994. Neural Networks for Pattern Recognition. Oxford University Press, Inc, New York.
Bishop, C.M., 2006. Pattern Recognition and Machine Learning. Springer Science+ Business Media, LLC, New York.
Chen, X., Kareem, A., 2003. New frontiers in aerodynamic tailoring of longspan bridges: an advanced analysis framework. J. Wind Eng. Ind. Aerod. 91, 1511–1528.
Chen, X., Matsumoto, M., Kareem, A., 2000. Aerodynamic coupling effects ON flutter and buffeting OF bridges. J. Eng. Mech. ASCE 17–26.
Chen, C.H., Wu, J.C., Chen, J.H., 2008. Prediction of flutter derivatives by artificial neural networks. J. Wind Eng. Ind. Aerod. 96, 1925–1937.
Cheynet, E., Jakobsen, J.B., Snæbjörnsson, J., 2016. Buffeting response of a suspension bridge in complex terrain. Eng. Struct. 128, 474–487.
Chopra, A.K., 2000. Dynamics of Structures. Prentice Hall, Upper Saddl River.
Cid Montoya, M., Nieto, F., Hernández, S., Kusano, I., Álvarez, A., Jurado, J., 2018. CFD-based aeroelastic characterization of streamlined bridge deck cross-sections subject to shape modifications using surrogate models. J. Wind Eng. Ind. Aerod. 177, 405–428.
Davenport, A.G., 1961. The spectrum of horizontal gustiness near the ground in high winds. Q. J. R. Meteorol. Soc. 87 (372), 194–211.
Davenport, A., 1962. Buffeting of a suspension bridge by storm winds. J. Struct. Div. 88 (3), 233–270.
Diana, G., Bruni, S., Rocchi, D., 2005. A numerical and experimental investigation on aerodynamic non. In: EACWE4 —The Fourth European & African Conference on Wind Engineering. Prage: Institute of Theoretical and Applied Mechanics Academy of Sciences of the Czech Republic, Prague, pp. 86–87.
Diana, G., Resta, F., Rocchi, D., 2008. A new numerical approach to reproduce bridge aerodynamic non-linearities in time domain. J. Wind Eng. Ind. Aerod. 96 (10–11), 1871–1884.
Fang, C., Tang, H., Li, Y., Zhang, J., 2020. Stochastic response of a cable-stayed bridge under non-stationary winds. Ocean Eng. 199 (106967), 1–15.
Fenerci, A., 2018. Full-scale investigation of the effects of wind turbulence characteristics on dynamic behavior of longs-span bridges in complex terrain. Trondheim: Doctoral theses at NTNU 100, 2018.
Fenerci, A., Øiseth, O., 2017. Measured buffeting response of a long-span suspension bridge compared with numerical predictions based on design wind spectra. J. Struct. Eng. 143 (9), 1–15, 04017131.
Fenerci, A., Øiseth, O., 2018. Strong wind characteristics and dynamic response of a long-span suspension bridge during a storm. J. Wind Eng. Ind. Aerod. 170, 116–138.
Fenerci, A., Øiseth, O., Rønnquist, A., 2017. Long-term monitoring of wind field characteristics and dynamic response of a long-span suspension bridge in complex terrain. Eng. Struct. 147, 269–284.
Fenerci, A., Kvåle, K. A., Petersen, Ø. W., Rønnquist, A., & Øiseth, O. (2018, 08 18). Retrieved from: https://doi.org/10.1016/j.engstruct.2017.06.069.
Hu, L., Xu, Y.-L., Huang, W.-F., 2013. Typhoon-induced non-stationary buffeting response of long-span bridges in complex terrain. Eng. Struct. 57, 406–415.
Hu, L., Xu, Y.-L., Zhu, Q., Guo, A., 2017. Tropical storm–induced buffeting response of long-span bridges: enhanced nonstationary buffeting force model. J. Struct. Eng. 143 (6).
Jain, A., Jones, N.P., Scanlan, R.H., 1996. Coupled aeroelastic and aerodynamic response analysis of long-span bridges. J. Wind Eng. Ind. Aerod. 69–80.
James, G., Witten, D., Hastie, T., Tibshirani, R., 2013. An Introduction to Statistical Learning with Applications in R. Springer Science+Business Media, New York.
Kaimal, J.C., Wyngaard, J.C., Izumi, Y., Cote, O.R., 1972. Spectral characteristics of surface-layer turbulence. Quaterly J. Roy. Meteorol. Soc. 98 (417), 563–589.
Katsuchi, H., Akiyama, H., Scanlan, R., Jones, N.P., 1998. Multi-mode flutter and buffeting analysis of the Akashi-Kaikyo bridge. J. Wind Eng. Ind. Aerod. 431–441.
Kuhn, H., Tuker, A., 1951. Nonlinear programing. In: Proceedings of the Second Berkeley Symposium on Mathematical Statistics and Probability. Berkeley.
Le, V., Caracoglia, L., 2020. A neural network surrogate model for the performance assessment of a vertical structure subjected to non-stationary, tornadic wind loads. Comput. Struct. 231.
Li, S., Laima, S., Li, H., 2018. Data-driven modeling of vortex-induced vibration of a long-span suspension bridge using decision tree learning and support vector regression. J. Wind Eng. Ind. Aerod. 172, 196–211, 2018.
Lystad, T.M., Fenerci, A., Øiseth, O.A., 2018. Evaluation of mast measurements and wind tunnel terrain models to describe spatially variable wind field characteristics for long-span bridge design. J. Wind Eng. Ind. Aerod. Elsevier 179, 558–573.
Lystad, T.M., Fenerci, A., Øiseth, O.A., 2020. Buffeting response of long-span bridges considering uncertain turbulence parameters using the environmental contour method, 213. Engineering Structures.
Macdonald, J., 2003. Evaluation of buffeting predictions of a cable-stayed bridge from full-scale measurements. J. Wind Eng. Ind. Aerod. 91 (12–15), 1465–1483.
McKay, M.D., Beckman, R.J., Conover, W.J., 1979. A comparison of three methods for selecting values of input variables in the analysis of output from a computer code. American Statistical Association and American Society for Quality, pp. 239–245.
Nieto, F., Cid Montoya, M., Hernández, S., Kusano, I., Casteleiro, A., Álvarez, A.J., et al., 2020. Aerodynamic and aeroelastic responses of short gap twin-box decks: box geometry and gap distance dependent surrogate based design. J. Wind Eng. Ind. Aerod. *201*.
Olsson, A., Sandberg, G., Dahlblom, O., 2003. On Latin hypercube sampling for structural reliability analysis. Struct. Saf. 47–68.
Petersen, Ø.W., Øiseth, O., Lourens, E.-M., 2017. Estimation of the dynamic response of a slender suspension bridge using measured acceleration data. In: X International Conference Oon Structural Dynamics. EURODYN 2017. Rome.
Ripley, B.D., 1996. Pattern Recognition and Neural Networks. Cambridge University Press, Cambridge ,UK.
Rizzo, F., Caracoglia, L., 2020. Artificial Neural Network model to predict the flutter velocity of suspension bridges. Comput. Struct. 233.
Rosenblatt, F., 1958. The perceptron: a probabilisitc model for information storage and organization in the brain. Psychol. Rev. 65 (6), 386–408.
Rosenblatt, F., 1961. Principles of Neurodynamics: Perceptrons and the Theory of the Brain Mechanisms. Spartan Books, Washington.
Rumelhart, D.E., Hinton, G.E., Williams, R.J., 1986. Learning representations by back-propagating errors. Lett. Nat. 323 (9), 533–536.
Scanlan, R.H., Tomko, J.J., 1971. Air foil and bridge deck flutter derivatives. J. Soil Mech. Found Div. 97 (6), 1717–1739.
Siedziako, B., Øiseth, O., Rønnquist, A., 2017. An enhanced forced vibration rig for wind tunnel testing of bridge deck section models in arbitrary motion. J. Wind Eng. Ind. Aerod. 164, 152–163, 2017.
Vapnik, V.N., 1995. The Nature of Statistical Learning Theory. Springer, New York.
Wang, H., Wu, T., 2020. Knowledge-enhanced deep learning for wind-induced nonlinear structural dynamic analysis. J. Struct. Eng. 146 (11).
Wang, H., Zhang, Y.-M., Mao, J.-X., Wan, H.-P., 2020. A probabilistic approach for short-term prediction of wind gust speed using ensemble learning. J. Wind Eng. Ind. Aerod. 202.
William, K., 1939. MInima of Several Variables with Inequalities as Side Conditions. University of Chicago, Chicago. Thesis (S.M.).
Wu, T., Kareem, A., 2011. Modeling hysteretic nonlinear behavior of bridge aerodynamics via cellular automata nested neural network. J. Wind Eng. Ind. Aerod. 99, 378–388, 2011.
Xu, Y.L., Zhu, L.D., 2005. Buffeting response of long-span cable-supported bridges under skew winds. Part 2: case study. J. Sound Vib. (281), 675–697.
Zhu, L.D., Xu, Y.L., 2005. Buffeting response of long-span cable-supported bridges under skew winds. Part 1: theory. J. Sound Vib. 281 (3–5), 647–673.